



Published in final edited form as:

*Cancer Res.* 2022 September 16; 82(18): 3209–3222. doi:10.1158/0008-5472.CAN-21-3914.

## GLS2 is a tumor suppressor and a regulator of ferroptosis in hepatocellular carcinoma

Sawako Suzuki<sup>1,2</sup>, Divya Venkatesh<sup>3</sup>, Hiroaki Kanda<sup>4</sup>, Akitoshi Nakayama<sup>5</sup>, Hiroyuki Hosokawa<sup>6</sup>, Eunyoung Lee<sup>7</sup>, Takashi Miki<sup>7</sup>, Brent R. Stockwell<sup>3,8, 1,2</sup>, Tomoaki Tanaka<sup>5,9</sup>, Carol Prives<sup>3,9</sup>

<sup>1</sup>)Department of Endocrinology, Hematology and Gerontology, Graduate School of Medicine, Chiba University, Chiba, Japan.

<sup>2</sup>)Department of Diabetes, Metabolism and Endocrinology, Chiba University Hospital, Chiba, Japan.

<sup>3</sup>)Department of Biological Sciences, Columbia University, New York, USA.

<sup>4</sup>)Department of Pathology, Saitama Cancer Center, Saitama, Japan.

<sup>5</sup>)Department of Molecular Diagnosis, Graduate School of Medicine, Chiba University, Chiba, Japan.

<sup>6</sup>)Department of Immunology, Tokai University School of Medicine, Kanagawa, Japan

<sup>7</sup>)Department of Medical Physiology, Chiba University, Graduate School of Medicine, Chiba University, Chiba, Japan.

<sup>8</sup>)Department of Chemistry, Columbia University, New York, USA

### Abstract

Glutamine synthase 2 (GLS2) is a key regulator of glutaminolysis and has been previously implicated in activities consistent with tumor suppression. Here we generated *Gls2* knockout (KO) mice that develop late-occurring B cell lymphomas and hepatocellular carcinomas (HCC). Further, *Gls2* KO mice subjected to the hepatocarcinogenic Stelic Animal Model (STAM) protocol produce larger HCC tumors than seen in wild-type mice. GLS2 has been shown to promote ferroptosis, a form of cell death characterized by iron-dependent accumulation of lipid peroxides.

<sup>9</sup>)Correspondence: Carol Prives, 816 Fairchild Building, Department of Biological Sciences, Columbia University, New York, NY 10027, clp3@columbia.edu, Tomoaki Tanaka 1-8-1 Inohana, Chuo-ku, Department of Molecular Diagnosis, Chiba University Graduate School of Medicine, Chiba, Chiba 260-8670, tomoaki@restaff.chiba-u.jp.

#### Authors Contributions

T.T. and S.S. initiated the project which was subsequently developed and further coordinated by C.P., D.V. and B.R.S. C.P. directed the work. C.P., D.V., T.T. and K.Y. designed the study. The manuscript was prepared by S.S., C.P. and D.V.. S.S. performed most of the experiments (*in vivo* data at Chiba university and *in vitro* data at Columbia university) and analyzed the data. D.V. helped design the experiments pertaining to ferroptosis and created the SKHep1 derived p53KO cells. H.K. performed the pathological analysis. A.N. analyzed data from the human Cancer Genome Atlas (TCGA) database. T.T. and H.H. created the *Gls2* knockout mice model. E.L. and T.M. aided with the animal experiments.

#### Authors Disclosures

B.R.S. is an inventor on patents and patent applications involving ferroptosis, holds equity in and serves as a consultant to Inzen Therapeutics and Nevrox Limited, and serves as a consultant to Weatherwax Biotechnologies Corporation, and Akin Gump Strauss Hauer & Feld LLP.

All other authors declare no potential conflicts of interest.

In line with this, GLS2 deficiency, either in cells derived from *Gls2* KO mice or in human cancer cells depleted of GLS2, conferred significant resistance to ferroptosis. Mechanistically, GLS2, but not GLS1, increased lipid ROS production by facilitating the conversion of glutamate to  $\alpha$ -ketoglutarate, thereby promoting ferroptosis. Ectopic expression of wild-type GLS2 in a human hepatic adenocarcinoma xenograft model significantly reduced tumor size; this effect was nullified by either expressing a catalytically inactive form of GLS2 or by blocking ferroptosis. Furthermore, analysis of cancer patient datasets supported a role for GLS2-mediated regulation of ferroptosis in human tumor suppression. These data suggest that GLS2 is a bona fide tumor suppressor and that its ability to favor ferroptosis by regulating glutaminolysis contributes to its tumor suppressive function.

---

## Introduction

Glutaminolysis, the stepwise process where glutaminase catalyzes the conversion of glutamine into glutamate (1), is an important pathway that intersects with several metabolic pathways such as glycolysis, TCA cycle, redox homeostasis, along with lipid and amino acid homeostasis (1–3). There are two glutaminase enzymes: glutaminase 1 (GLS1) and glutaminase 2 (GLS2) (4). While GLS1 is regulated by the oncogenes MYC (5), Rho GTPases (6) and Notch (7), we and another group previously reported that the p53 tumor suppressor protein activates the transcription of GLS2, which positively regulates aerobic energy production in mitochondria and suppresses the simultaneously produced oxidative stress (8, 9). Since the two glutaminase enzymes appear to play opposite roles in tumorigenesis, switching between GLS1 and GLS2 is attracting attention as a new cancer target (10–15). While GLS1 is well validated as a cancer promoter (6, 7, 16, 17), the tumor suppressor functions of GLS2 have not been studied extensively, although one study has reported that GLS2 can inhibit the small GTPase Rac1 by direct binding (18). We previously reported that the expression of GLS2 is reduced in liver tumors and that ectopically expressed GLS2 reduces the growth and colony forming ability of tumor cells (8). Consistent with our reports, overexpression of GLS2 has also been reported to suppress the malignant phenotype (8, 9, 19–21) and sensitize glioma cells to chemotherapeutic alkylating agents (20). Yet, in other studies it was reported that knockdown of GLS2 inhibits the growth of cervical cancer cells (22) and sensitizes human hepatoma and lung carcinoma to ionizing radiation (23). Thus, the tumor suppressor function of GLS2 appears to be complex and dependent on the cancer cell types used for different *in vitro* studies. Most relevantly, it is still unclear whether and how GLS2 acts as a tumor suppressor *in vivo* and what mechanisms enable it to do so.

Recently, Gao, et al. reported that GLS2 is involved in an iron and lipid peroxide-dependent cell death, termed ferroptosis (24), which has been suggested to be associated with cancer suppression (25–27). In fact, Jennis M et al. (28) generated mice expressing a p53 variant that is defective in expression of *Gls2*, and such mice are deficient in undergoing ferroptosis. Ferroptosis, which can be initiated by small molecules (FINs) such as erastin and IKE (Imidazole Ketone Erastin-a more potent form of erastin), involves the eventual inhibition of cellular antioxidant defenses such as glutathione peroxidase 4 (GPX4) and co-enzyme Q<sub>10</sub> leading to accumulation of lipid peroxides. This type of cell death is suppressed by

lipophilic antioxidants such as ferrostatin-1 (Fer-1) (29, 30). Recent studies have revealed that certain FINs inhibit tumor growth and can be combined with traditional methods of cancer therapy, especially for resistant cancers (25–27). Although the exact mechanism by which ferroptosis inhibits tumor growth is still unknown, different lines of evidence suggest that such FINs may be used to treat tumor cells and ultimately cancer.

In the present study, we generated *Gls2* knockout (KO) mice to determine whether these mice develop tumors and to investigate a possible association of GLS2 with ferroptosis in this setting. We have also discovered that failure of energy homeostasis via glutaminolysis is involved in tumorigenesis caused by lack of GLS2.

## Materials and Methods

### Animals.

$Gls2^{tm1a(EUCOMM)Wtsi}$  ES cell lines were obtained from the International Knockout Mouse Consortium (KOMP, [www.KOMP.org](http://www.KOMP.org)). The targeting vector, containing an IRES-*lacZ* trapping cassette and floxed *neo* cassette, was inserted into the first intron of the *Gls2* gene, resulting in disruption of functional *Gls2* transcription. The targeting vector was introduced into C57BL/6N ES cells and the mice bearing a null mutation of *Gls2* alleles were generated as described previously (31).

STAM, a non-alcoholic steatohepatitis (NASH)-cirrhosis-hepatocarcinogenic model (Stelic Institute & Co., Tokyo, Japan), was used for hepatocarcinogenetic experiments. Briefly, 2-day-old male pups were injected with streptozotocin (200  $\mu$ g per mouse) and fed a high-fat diet (D12492, Research Diet Inc.) from the age of 4 weeks. This mouse model progressed from non-alcoholic fatty liver disease (NAFLD) to NASH at 8 weeks of age and developed hepatocellular carcinoma at 16–20 weeks of age. The background liver histology of the STAM model was assessed by using the NASH score that includes fatty change, lobular inflammation, ballooning, sinus dilatation and fibrosis. Livers including tumors were cut at 5–7mm intervals. If there were no large tumors, 6 slices were made per whole liver. All sliced samples were examined histologically and every tumor was confirmed hepatocellular carcinoma or lymphoma by the pathologist.

The mice were maintained under specific pathogen-free conditions, on a 12-hour light-dark cycle, fed a normal diet (CE-2, Clea Japan Inc) or high-fat diet (D12492, Research Diet Inc.) ad libitum. Only male mice were used for experiments. All animal studies were conducted in accordance with the International Guiding Principles for Biomedical Research Involving Animals and were approved by the Animal Care and Use Committees of Chiba University and the National Institute for Physiological Sciences in Japan.

### Genotyping.

*Gls2*-deficient mice were genotyped by PCR using P1 primer, 5'-cccatatctgttcagttctccagg-3', and P2 primer, 5'-ttgctcaaggccaactcacagttc-3'. The PCR products are 365 bp for the wild-type allele, and 334 bp for the mutant allele.

### Primary hepatocyte culture, cell lines and reagents.

Primary hepatocytes were prepared by perfusing the portal vein of the liver with 95  $\mu\text{g/ml}$  EGTA, 150 U/ml collagenase solution and enriched using a 36% Percoll (Sigma-Aldrich) gradient. Hepatocytes were cultured in Hepatocyte Culture Medium (COSMO BIO) on collagen-coated 6-well plates. SKHep1 p53KO cells were generated using CRISPR/Cas9 genome editing as previously described (32). HepG2 (wild-type p53-positive hepatocellular carcinoma) and HepG3 (p53-null hepatocellular carcinoma) cell lines were purchased from ATCC (LCG Standards GmbH, Wesel, Germany).

Probucol,  $\alpha$ -ketoglutarate ( $\alpha\text{KG}$ ), glutamate (Glu), amino-oxyacetate (AOA), and ferrostatin-1 (Fer-1) were purchased from Sigma Aldrich. Erastin was purchased from Selleckchem. Liproxstatin-1 and deferoxamine (DFO) were purchased from Funakoshi. IKE was synthesized in the lab of Dr. Brent Stockwell as in Larraufie et al (33).

### Plasmid Construction, Recombinant Virus Production, and Transduction.

Full-length human GLS2 (NM\_013267;1809 bp) was subcloned into the p3 $\times$ FLAG-CMV10 vector (Sigma-Aldrich), pAcGFP1-N1 (Addgene), or CSII-EF-RfA-IRES2-Venus (RDB4389, Riken BioResource Center). We used PCR to generate a GLS2 glutaminase core domain deletion mutant, in which amino acids 177–468 are deleted from the full-length GLS2.

FLAG-tagged plasmids expressing wild-type hGLS2 (GLS2<sup>WT</sup>) or the 177–468 deletion mutant (GLS2<sup>del</sup>) in 3 $\times$ FLAG-CMV10, or 3 $\times$ FLAG-CMV10 (empty vector (Mock)) or pAcGFP1-N1-GLS2 were transfected into SKHep1 p53KO cells using Lipofectamine<sup>®</sup> 3000 (Invitrogen), as described in the manufacturer's protocol.

We produced recombinant lentiviruses and the lentivirus vector-containing culture supernatant as described previously (34). SKHep1 p53KO cells were infected with either CSII-EF-RfA-IRES2-Venus-empty vector (Mock) as well as GLS2<sup>WT</sup>- or GLS2<sup>del</sup>-containing CSII-EF-RfA-IRES2-Venus lentiviruses. Three days after infection, GFP-positive lentivirus-infected cells were sorted with a FACSAria (Becton Dickinson).

To generate lentivirus-based shRNA constructs, a 19 bp shRNA-coding fragment with a 5'-ACGTGTGCTGTCGGT-3' loop was introduced into pENTR4-H1 digested with BgIII/XbaI. To insert the hGLS2 or hGLS1-shRNA into the lentivirus vector, we mixed the resulting pENTR4-H1-shRNA vector and CS-RfA-CG vector with Gateway LR clonase (Invitrogen). The GLS2 or GLS1 target sequences are CTCCATAAGCACCTAGGC or AAGAGAAAGTGGAGATCGA, respectively. SKHep1 WT cells were infected with either empty vector (shCont) or shGLS2 / shGLS1-containing CS-RfA-CG lentiviruses.

### RNA interference.

21 nucleotide siRNA duplexes with 3' dXdY overhangs corresponding to hGLS2 mRNA (GLS2 RNAi, 5' - ATCAAGATGGACTGTAACAAA -3') or hGLS1 mRNA (GLS1 RNAi, 5' - AAGAGAAAGTGGAGATCGAAA-3') or firefly luciferase mRNA for control RNAi (luciferase, 5' -AACTTACGCTGAGTACTTTCGA-3') were synthesized by QIAGEN Inc. (Valencia, CA). SKHep1 WT cells were transfected with the indicated siRNA

oligonucleotide (40 nM) using Lipofectamine<sup>®</sup> 3000 (Thermo Fisher Scientific, Inc.) reagent according to the manufacturer's protocol.

#### Measurement of cell viability.

Cell viability was measured by normalizing ATP levels using the Cell Titer-Glo reagent as previously described (8). Cell viability was normalized to the corresponding DMSO-treated control cells and presented as a percentage of the control.

#### Measurement of reactive oxygen species (ROS) and intracellular Fe<sup>2+</sup>.

Cells were incubated with, C11-BODIPY (2 μM), Mitosox (5 μM) or 2',7'-dichlorodihydro-fluorescein diacetate (DCF; 3 μM) for lipid ROS, mitochondrial ROS or cytosolic ROS respectively and measured in IncuCyte<sup>®</sup> live-cell analysis system. All ROS reagents were purchased from Molecular Probes, Invitrogen. Fe<sup>2+</sup> was assessed with the turn-on FeRhoNox<sup>™</sup>-1 fluorescent probe as described by Hirayama et al. (35) and obtained from Goryo Chemical Inc. (Goryo, Japan).

#### Quantitative RT-qPCR.

RT-qPCR was performed as described (8). All gene-specific mRNA expression values were normalized against the internal housekeeping gene, 18S for mice and L32 for humans. Please see Supplementary information for primer sequences.

#### RNA-sequencing analysis.

Total RNA (10 μg) from each sample was prepared as previously described (36). The resulting size-fractionated cDNA was used for sequencing with an Illumina GAIIx. The generated sequence tags were mapped onto the human genome sequence (mm9 from the UCSC Genome Browser) using the Eland program (Illumina). Unmapped or redundantly mapped sequences were removed from the dataset, and only uniquely mapped sequences without any mismatches were used for analyses. Gene expression was quantified as Fragments Per Kilobase Million (FPKM) (37).

#### Western blot analysis and antibodies.

We performed Western blot analyses as previously described (8). The primary antibodies for mouse samples were as follows: GlS2 (Abcam), GlS1 (Abcam), Caspase-3 (Abcam), p53 Ab3 (Merk), and β-actin (Sigma-Aldrich). The primary antibodies for human samples were as follows: M2-FLAG (Sigma-Aldrich), p53 DO1 (Santa Cruz Biotechnology) anti-actin (Sigma). A polyclonal antibody, hGLS2 (N14), was raised against human GLS2 protein (TaKaRa) using a synthetic peptide (corresponding to a sequence within the GLS2 N terminus: PSHSQPQHGDHDSS) conjugated to KLH. The titer of the crude rabbit sera was confirmed by ELISA and then the sera were subjected to affinity purification using recombinant hGLS2 protein as previously described (8).

#### Metabolomic analysis.

Extracts were prepared from  $\sim 2 \times 10^6$  cells with methanol containing internal standard solution (Human Metabolome Technologies). Cationic compounds were measured in the

positive mode of capillary electrophoresis–connected time-of-flight mass spectrometry (CE-TOFMS) and anionic compounds were measured in the positive and negative modes of CE-MS/MS.

### **Determination of glutamate and glutamine concentrations.**

Concentrations of glutamate and glutamine in the medium were determined using a glutamine/glutamate determination kit (GLN-1; Sigma-Aldrich) as previously described (8).

### **Oxygen consumption assays.**

One day following transfection with p3×FLAG-CMV10-hGLS2 constructs or p3×FLAG-CMV10-empty vector (Mock), equal numbers of cells in KRH buffer (Krebs-Ringer Hepes buffer; 25 mM Hepes, 130 mM NaCl, 5 mM KCl, 1.3 mM CaCl<sub>2</sub> and 1.3 mM MgSO<sub>4</sub>, pH 7.4) supplemented with 2.5% BSA and 2 mM sodium pyruvate were seeded in triplicate into BD Oxygen Biosensor System (BD Biosciences, San Diego, CA). Oxygen consumption was measured in a fluorescence plate reader at 485 nm excitation and 630 nm emission at 2-hour intervals for 24 hours.

For measurement of mitochondrial respiration (Seahorse Biosciences), SKHep1 cells were cultured overnight on XFe 96 plates at a density of 20,000 cells per well. Then the medium was replaced 1 hour before the start of the measurement of mitochondrial respiration. Oligomycin (2 μM), carbonilcyanide p-trifluoromethoxyphenylhydrazone (FCCP, 0.5 μM), antimycin (0.5 μM), and rotenone (1 μM; Sigma) were added to XFe 96 media, and the samples were loaded into the sensor cartridge. Oxygen consumption rate (OCR) was then recorded by using a XF24 extracellular flux analyzer.

### **Metabolic studies.**

For the oral glucose tolerance test (OGTT), insulin tolerance test and pyruvate tolerance test, 16–20 weeks old mice were fasted for 16 hours and then glucose (1 g/kg) was administered orally, insulin (0.75 IU/kg) and sodium pyruvate (1 g/kg) was administered intraperitoneally (38). Blood glucose concentrations were measured at the indicated time points using a glucometer (Glutestmint; Sanwa Kagaku Kenkyusho Co. Ltd.).

### **Xenograft model of tumor growth suppression assay in animals.**

For assessment of tumor growth suppression, a total of  $1 \times 10^5$  of SKHep1 p53KO cells infected with CSII-EF-RfA-IRES2-Venus lentiviruses containing either GLS2<sup>wt</sup> / GLS2<sup>del</sup> or CSII-EF-RfA-IRES2-Venus-empty vector constructs (Mock) and SKHep1 cells with either CS-RfA-CG -empty vector (shCont) or shGLS2 / shGLS1 constructs, were suspended in 50 μl of DMEM with 50 μl Matrigel (BD Biosciences). Subcutaneous injections of SKHep1 cells with indicated vector constructs were performed on the right and left flanks of the same SCID mice (5–6 weeks, male; Clea Japan Inc). Six weeks after subcutaneous injections, tumors were dissected and GFP expressed from lentiviral vector was measured using the IVIS imaging system (Perkin Elmer) according to the manufacturer's protocol (Perkin Elmer). Although both the Institutional Animal Care and Use Committee protocols demand that the maximal tumor size should not exceed 2 cm in any dimension, none of the implanted tumors in our experiments exceeded this restriction.



### Colony formation assay, transwell invasion assays and wound healing assays.

Colony formation assays were performed as previously described (39) and invasion assays were performed using transwell invasion chambers coated with Matrigel (50  $\mu$ l per filter) (BD Biosciences, Franklin Lakes, NJ, USA) as described in the manufacturer's protocol. SKHep1 p53KO cells were transfected with either p3 $\times$ FLAG-CMV10-GLS2<sup>WT</sup>, p3 $\times$ FLAG-CMV10-GLS2<sup>del</sup> or p3 $\times$ FLAG-CMV10-empty vector constructs (Mock) and cultured for 48 hours prior to being transferred onto the top of Matrigel-coated invasion chambers with 1% FBS DMEM (5 $\times$ 10<sup>4</sup> cells/well). DMEM containing 10% FBS was added to the lower chambers. After incubation for 24 hours at 37°C in an atmosphere containing 5% CO<sub>2</sub>, invaded cells on the lower surface were stained with crystal violet stain and counted under a light microscope. For wound scratch assays, transfected cells were cultured on collagen I (BD Biosciences) until confluence and then wounded using a blue 1ml pipette tip (40). Media was removed, cells washed with PBS, and replenished with fresh media. Images were acquired immediately following media replacement, and after 24 h via phase-contrast microscope at 10 $\times$ . After exporting images, wound areas were measured using ImageJ.

### Histological examination.

Hematoxylin and eosin staining were performed as previously described (39). 4-HNE, a highly toxic aldehyde product of lipid peroxidation, was evaluated using an anti-4-HNE monoclonal antibody (bs-6313R, Bioss Inc.) and labeled DAKO EnVision + System-HRP Labelled Polymer Anti-Rabbit. Oil-Red O staining was performed in frozen liver sections as previously described (41). Sirius red staining for collagen deposition was performed as previously referenced (42). The primary antibodies for mouse samples were as follows: GlS2 (Sigma-Aldrich) and p53 Pab240 (Santa Cruz Biotechnology Inc). The slides were examined under a Keyence BZ-8100 microscope (Keyence Japan, Osaka, Japan).

### Methylation-specific PCR assay.

The methylation-specific PCR assay for the *GlS2* promoter was performed as previously described (43). Genomic DNA was purified from tumor tissues using the DNeasy Blood and Tissue Kit (Qiagen, Valencia, CA, USA). For DNA bisulfite modification, we used the DNA modification kit (Epigentek Inc., New York, NY, USA) according to the manufacturer's protocol. Primers for RT-qPCR analyses of live mice samples for DNA bisulfite modification analyses were as follows: mGlS2 methylated oligonucleotides, 5' - gatttaagaatttggtttatgac -3' and 5' - caatacacttacaacaacgat -3'; mGlS2 unmethylated oligonucleotides, 5' - tgatttaagaatttggtttatgac -3' and 5' - aaccaatacacacttacaacaaca -3'. Amplified total DNA was subjected to electrophoresis on a 2% agarose gel, and then visualized by ethidium bromide staining.

### Statistics.

Results are expressed as means  $\pm$  SEM. Differences between two groups were assessed using the unpaired two-tailed Student's t-test. P < 0.05 was considered to be statistically significant.

## Data Availability

The data generated in this study are available upon request from the corresponding author.

## Results

### ***Gls2* knockout mice exhibit markedly a increased incidence of hepatocellular carcinoma**

Since GLS2 proteins share a high degree of homology (98%) between human and mice (Supplementary Fig. S1A), we generated *Gls2* knockout mice (KO) to further study the functional roles of GLS2 *in vivo*. The gene targeting strategy for the generation of the KO mice is shown in Supplementary Fig. S1B. Briefly, a gene trap vector was inserted into introns 1 and 7 to delete exons 2–7 after Cre-mediated gene recombination. The targeting vector was electroporated into ES cells, and upon establishing cells that had undergone homologous recombination, KO mice were successfully generated (Supplementary Fig. S1C). In these KO mice, Gls2 protein and mRNA expression were ablated while levels of Gls1 protein remained unchanged (Fig. 1A, Supplementary Fig. S1D and S1E). These expression changes were assessed in the livers of mice, since the liver possesses the highest expression of GLS2 amongst all the organs examined in both mice and humans (Supplementary Fig. S2A and S2B). The KO mice were born at Mendelian ratios (Supplementary Fig. S2C), with no external malformations. When wild-type (WT) and KO mice were sacrificed over time, however, we found that by 120 weeks of age, all seven KO mice examined had developed tumors – four of these exhibited B cell lymphomas, two had hepatocellular carcinomas (HCCs) and one had both HCC and B cell lymphoma (Fig 1B and 1C). By contrast, none of the six WT mice examined exhibited any tumors at 120 weeks of age (Fig. 1B and 1D). When the hepatocellular carcinomas in the KO mice were segregated into size-based categories (under 1 mm, 1–3 mm and above 3 mm pathologically; Fig. 1E), two out of the three HCCs in the KO mice were relatively large tumors that exceeded 3 mm pathologically (Fig. 1F). This indicates that the absence of GLS2 significantly increases the onset of liver tumors albeit at a later stage in murine life, and further enables the tumors to grow in size.

Next, to confirm that GLS2 loss was involved in the development of liver cancer, we created STAM mice (44), which is a model for non-alcoholic steatohepatitis (NASH) leading to HCC. STAM mice (C57BL/6 strain) were established by using a combination of chemical (subcutaneous injection of low dose streptozotocin) and subjecting mice to a high-fat diet (Fig. 1G). These interventions resulted in marked hyperglycemia with low insulin secretion, hypercholesterolemia, and high alanine aminotransferase (ALT) levels (Supplementary Fig. S3A-S3D). The protocol also resulted in progression from fatty liver to NASH by 8 weeks of age, followed by cirrhosis and finally, development of HCC in all the mice by 20 weeks of age (Fig. 1G, Supplementary Fig. S3E). At 15 weeks of age, macroscopically clear liver masses were already observed in the *Gls2* knockout STAM (KO-STAM) mice but not in wild-type STAM (WT-STAM) mice (Fig. 1H). Subsequent pathological analysis revealed that the KO-STAM mice also showed an increase in number of large HCCs (above 3 mm) when compared to WT-STAM mice (Fig. 1I). Neither the presence of small HCCs (below 3mm) nor NASH scores differed between the two groups (Supplementary Fig. S3F). Taken together, we surmise that the loss of GLS2 contributes to an earlier onset of tumors, be



it spontaneously or under stress; further our data also suggest that GLS2 loss significantly promotes progression of liver tumors.

### Hepatocellular carcinomas exhibit a weak ferroptotic response in the absence of GLS2

Since we previously reported that GLS2 can provide an antioxidant effect *in vitro*, we hypothesized that probucol, a drug with antioxidant properties (45) and reported to have a protective effect on liver stenosis and NASH (46, 47), might suppress the development of HCC in KO-STAM mice. Unexpectedly, and contrary to our original hypothesis, the KO-STAM mice with probucol mixed into their high-fat diets (KO-STAM with probucol) showed *exacerbated* HCC (Fig. 1H and Fig. 1I). This counterintuitive result suggested that the formation of HCC in the KO mice could not simply be a result of increased oxidative stress. As GLS2 was previously shown to favor ferroptosis (24, 48, 49), and as probucol has been recently shown to be an inhibitor of ferroptosis (50), we hypothesized that failure to induce ferroptosis in our KO mice might be involved in the onset of hepatocellular carcinoma (51).

For the rest of this study we have employed several experimental approaches to examine ferroptosis: First, since reagents such as antibodies that can identify cells undergoing ferroptosis are not easily available, where appropriate we have evaluated the expression of established ferroptosis markers such as 4-Hydroxynonenal (4-HNE), *Ptgs2* and *Chac1* (52, 53). Second, we have used both primary hepatocytes from *Gls2* knockout mice and the human cell lines (SKHep1 WT, HepG2 and Hep3B) that were initially derived from human hepatocellular carcinomas in order to examine the interplay between GLS2 and ferroptosis. Finally, we have used the two different classes of ferroptosis inducers (erastin/IKE and RSL3) to cause cell death as measured by an ATP-based cell viability assay and we have confirmed that this death is ferroptosis by demonstrating that it can be inhibited by the ferroptosis specific inhibitors (ferrostatin, liproxstatin and deferoxamine) (48, 49) as well as by confirming the associated increase in lipid ROS prior to the start of cell death.

We observed that ferroptosis markers, 4-HNE and *Ptgs2*, were increased in liver tumors from WT-STAM compared to tumors from KO-STAM or non-tumors (Fig. 1J and 1K). We next performed the Malondialdehyde (MDA) assay to measure the end products of lipid peroxidation, the inducer of ferroptotic death, and showed that MDA was significantly decreased in the livers from KO compared to WT mice (Fig. 2A). Additionally, primary hepatocytes from the KO mice also showed decreased sensitivity to inducers of ferroptosis when compared to hepatocytes derived from WT mice (Fig. 2B and 2C). These altered levels of cell death in the hepatocytes were fully attenuated by the ferroptosis inhibitor, Fer-1 (Fig. 2B and 2C) and were not associated with changes in the levels of the apoptosis marker, cleaved caspase-3 (Supplementary Fig. S4A), thereby confirming that the cell death seen was in fact due to ferroptosis. Since the HCC lesions in WT-STAM were more resistant to ferroptosis compared to the non-HCC lesions (Supplementary Fig. S4B and S4C), this supports the possibility that the livers of KO mice have properties similar to HCC. Further, the ferroptosis resistance observed in primary hepatocytes from KO mice was attenuated by overexpression of wild-type GLS2, supporting our conclusion that GLS2 is essential for complete ferroptosis induction in primary hepatocytes (Fig. 2D and 2E).

To further evaluate the relationship between tumorigenesis and ferroptosis as well as to other forms of programmed cell death such as autophagy and apoptosis in KO mice, RNA-sequencing analysis was performed in non-HCC liver tissues of WT mice and KO mice as well as in HCCs derived from 120-week-old KO mice (Supplementary Fig. S4D). Expression of several genes related to autophagy and apoptosis was generally increased in the non-HCC samples from the KO compared to WT mice. In the HCCs from the KO mice, expression of autophagy-related genes tended to decrease, while apoptosis-related genes showed varying trends that differed with the gene that was assayed. Note that the ferroptosis-related gene, *Ptgs2* was expressed in the WT mice, while *Ptgs2* expression was completely abolished in both non-HCC and HCC from KO mice. (Fig. 2F). Given that autophagy has also been shown to accompany death due to ferroptosis (54, 55), these data together demonstrate that ferroptosis induction was downregulated in HCCs from the KO mice. Finally, we confirmed that a high dose of probucol was able to substantially suppress erastin-induced ferroptosis in human SKHep1 cells in agreement with a published report (50) (Supplementary Fig. S5A and S5B). Together these *in vitro* data suggest that probucol exacerbates HCC in the KO-STAM mice most likely by *further* inhibiting ferroptosis *in vivo*. Taken together, our data indicate that ferroptosis is involved in the onset and progression of HCC in *Gls2* KO mice.

### GLS2 but not GLS1 can facilitate ferroptosis by promoting lipid ROS formation

To investigate the mechanism by which GLS2 might potentiate ferroptosis we used human SK-HEP-1 cells from which either GLS1 or GLS2 were depleted using siRNAs (Fig 3A). When these cells were treated with erastin, ablation of GLS1 did not significantly reduce the degree of cell death over 24 hours compared to control siRNA (Fig. 3B, Supplementary Fig. S6A and S6B). By contrast, when GLS2 was silenced in these cells, ferroptotic death was reduced as evidenced by the time of death onset, the lethal concentration of erastin and maximum amount of cell death achieved at the higher erastin concentration; with the most significant differences observed at 18 and 24 hours after erastin treatment (Fig 3B and Supplementary S6B). Conversely, under normal conditions, GLS2-silenced cells actually showed a decrease in viability as measured by ATP levels (Fig. 3B right panel).

We then analyzed the effect of GLS2 on lipid ROS and intracellular  $\text{Fe}^{2+}$  levels, which are the main ferroptosis mediators. We used C11-BODIPY to calculate the ratio of oxidized (green) to non-oxidized (red) forms of lipids in order to assess lipid ROS (56). Ablation of GLS2 in the SKHep1 cells caused a decrease in lipid ROS at 12 hours post-treatment with erastin, even though at this time point ferroptotic death was still not pronounced. The decrease in lipid ROS became even more significant at 18 hours post erastin treatment when there was observable death in the control cells (Fig. 3C and 3D). No such decrease in lipid ROS was observed in GLS1-silenced cells compared to the control. On the other hand, GLS2 silencing did not affect intracellular  $\text{Fe}^{2+}$  levels after erastin treatment suggesting that GLS2 functions downstream of labile iron production or release (Fig. 3E and 3F). We extended these findings to a second human hepatocellular carcinoma cell line (HepG2), where ferroptotic death and lipid ROS were partially rescued by GLS2 silencing after treatment with both class I and class II ferroptosis inducers (erastin and RSL3) (Fig. 3G and 3H).

We previously reported that GLS2 exerts antioxidant activity via GSH (8), and here we found that silencing of GLS2 modestly reduced the GSH / GSSG ratio in SKHep1 cells (Supplementary Fig. S6C). However, when erastin was administered to induce ferroptosis, the GSH / GSSG ratio was markedly depleted as previously reported (52) (Supplementary Fig. S6D). Note that the depletion of GSH under erastin was much more extensive than that seen with the knockdown of GLS2 (Supplementary Fig S6C and S6D). Although we had found that reducing GLS2 leads to GSH depletion, lowering GLS2 also inhibited ferroptosis, causing a concomitant decrease in lipid ROS. As an explanation, we believe that the antioxidant function of GLS2 via enhancing GSH levels is not of much consequence in the context of ferroptosis. Instead, we hypothesize that the role of GLS2 in promoting the accumulation of lipid ROS is dominant in that setting. We propose that there is a shift in the roles of GLS2 when ferroptosis is induced and we provide support for this theory below.

### **GLS2 promotes $\alpha$ -ketoglutarate production through glutamate and thereby increases lipid ROS during ferroptosis**

Next, to clarify the role of GLS2 in regulation of lipid ROS, we asked whether GLS2 promotes aerobic energy production through the TCA cycle, which has been reported to influence ferroptosis through mitochondrial membrane hyperpolarization (57).

To approach this experimentally, we used p53 knockout clones that were derived from SKHep1 cells by using CRISPR/Cas9 methodology (SKHep1 p53KO) (58) as they were more resistant to ferroptosis compared to SKHep1 WT cells (Fig. 4A) as reported in previous papers (32, 59–61). These cells are expected to be unable to induce the expression of GLS2 in response to stressors owing to the absence of p53 (8). In line with this, we found that GLS2 protein (Fig 4B; upper panel) and mRNA (Fig 4B; lower panel) levels were increased in response to ferroptosis in SKHep1 WT but not in p53 KO cells, suggesting that insufficient induction of GLS2 in the p53 KO cells can contribute to this resistance. The ferroptosis markers, *PTGS2* and *CHAC1* were induced these cell lines, consistent with the induction of ferroptosis in both WT and p53 KO cells (Fig. 4C). These data indicate that GLS2 might respond to the induction of ferroptotic stress also only in the presence of p53. Therefore, we ectopically expressed GLS2 in SKHep1 p53KO cells (Fig. 4D) and ablated GLS2 using siRNA in SKHep1 WT cells (Fig. 3A) to analyze associated cellular changes and response to ferroptosis induction.

This exogenous GLS2 displayed pronounced colocalization with that of the mitochondrial-specific stain, mitotracker indicating that it resembled the functioning of endogenous GLS2 (Fig. 4E). Further, overexpression of GLS2 modestly but significantly increased oxygen consumption while the silencing of GLS2 decreased oxygen consumption, which in turn reflects mitochondrial activity through the TCA cycle and electron transport (Fig. 4F). Thus, we hypothesized that GLS2 might be able to control the TCA cycle and thereby influence ferroptosis via  $\alpha$ -ketoglutarate production that is catalyzed by GLS2. In line with this, when we performed metabolomic analysis with the GLS2-silenced SKHep1 cells that showed increase ferroptosis resistance (Fig. 3) had lower levels of  $\alpha$ KG, and the ensuing ratio of  $\alpha$ KG to glutamate was also diminished (Fig. 4G, Supplementary Fig. S7), even though changes in the levels of glutamate and glutamine were subtle (Supplementary Fig. S7).

In line with the above hypothesis, under normal conditions, the observed modest decrease in viability of cells due to GLS2-silencing (Fig. 3B and 3G) was abolished by the addition of  $\alpha$ KG or glutamate (Glu), without affecting cellular morphology in both SKHep1 WT (Fig. 4H and 4I) and HepG2 cells (Fig. 4J and Supplementary Fig. S8A). The increased resistance to erastin-induced ferroptosis by GLS2 silencing in these cells was also lost upon the co-addition of either  $\alpha$ KG or glutamate (Fig. 4H, 4I and 4J). While the addition of AOA,  $\alpha$ KG or glutamate also accordingly altered the lipid ROS levels in these cells (Supplementary Fig. S8B and S8C), the intracellular  $\text{Fe}^{2+}$  levels were not affected under any of these conditions (Supplementary Fig. S8D).

On the other hand, the overexpression of GLS2 in two human cancer cell lines lacking p53 expression (SKHep1 p53KO cells and p53-null hepatocellular carcinoma Hep3B cells) enhanced their sensitivity to ferroptosis at 24 hours after erastin treatment with a concomitant increase in the levels of lipid ROS (Fig. 4K, 4L, 4M, Supplementary Fig. S8E, S8F, S8G and S8B). These effects of GLS2 overexpression were reduced by the administration of ferroptosis inhibitors Fer-1, Liproxstatin-1 as well as DFO (deferoxamine) (Fig. 4N) as well as amino-oxyacetate (AOA) (62), which inhibits the conversion of glutamate to  $\alpha$ KG (Fig. 4K, 4L, 4M, Supplementary Fig. S8E and S8F). Note that while the overall cell survival even with the ferroptosis inhibitors is lower under GLS2 overexpression, these inhibitors provide a similar degree of increase in viability under both control and GLS2 overexpression conditions and the overall reduction in cell viability is probably a function of the stoichiometric relationship of the inhibitors with the death. In contrast, under normal conditions, GLS2-overexpressed cells showed a small but significant increase in viability as measured by ATP levels, but this increase was also nullified by the administration of AOA treatment (Fig. 4L and 4M). Note that the ability of iron chelator, DFO to suppress the effects of GLS2 overexpression similar to inhibitors of lipid peroxidation (Fer-1, Liproxstatin-1) further suggests that GLS2 affects molecular pathways involved ferroptosis that are downstream of the production or release of labile iron.

Based on these findings that the ferroptosis response of human cancer cells can be altered by modulating the levels of GLS2 and  $\alpha$ KG, we propose that GLS2 induces lipid ROS-dependent ferroptosis by regulating mitochondrial function through production of  $\alpha$ KG.

### **GLS2 responds to the induction of ferroptosis, modulates cell death and suppresses tumorigenesis via its glutaminase core domain**

The GLS2 protein consists of 603 amino acids and its glutaminase core domain is located between positions 177–463 (Supplementary Fig. S9A). To determine whether the glutaminase core domain is important for the ability of GLS2 to promote ferroptosis and tumor suppression in SKHep1 p53KO cells we constructed a mutant form of GLS2 that lacks residues 177–463 (GLS2<sup>del</sup>) (Fig. 5A). When full-length wild-type human GLS2 (GLS2<sup>wt</sup>) or GLS2<sup>del</sup> were ectopically expressed in SKHep1 p53KO cells, as expected only GLS2<sup>wt</sup> increased glutamine consumption and glutamate production in the medium (Supplementary Fig. S9B and S9C). When we examined the oxygen consumption rate (OCT) using the flux analyzer, the increase in oxygen consumption due to the expression of GLS2<sup>wt</sup> in SKHep1 p53KO cells was completely abolished when GLS2<sup>del</sup> was expressed

instead (Fig. 5B). Notably, GLS2<sup>wt</sup> but not GLS2<sup>del</sup> suppressed colony formation in soft agar, cell invasion and cell migration (Supplementary Fig. S9D, S9E and S9F). Thus, the glutaminase core domain is essential for the tumor suppressive functions of GLS2. Importantly as well, expression of GLS2<sup>del</sup> was unable to mimic the ability of GLS2<sup>wt</sup> expression to enhance erastin-induced ferroptosis (Fig. 5C and Supplementary Fig. S9G).

We then created a xenograft model with the SKHEP1 p53KO cells to express the two variants of GLS2 using lentiviral vectors (Fig. 5D). In this setting, GLS2<sup>wt</sup> expressing cells resulted in significantly smaller tumors at six weeks after subcutaneous injection into SCID mice when compared to injections of either control (Mock) cells or cells expressing GLS2<sup>del</sup> (Fig. 5E and 5F). The tumor growth inhibitory effects of GLS2<sup>wt</sup> were accompanied by an increase in the expression of ferroptosis markers in SCID mice, which was lost if replaced by GLS2<sup>del</sup> (Fig. 5F). Of key importance the growth suppressive abilities of GLS2<sup>wt</sup> cells as well as the induction of ferroptosis markers were abolished by treatment with the ferroptosis inhibitor Fer-1 (Fig. 5G and Fig. 5H). In addition, we confirmed that shGLS2 expressing SKHep1 cells (also created using lentiviral constructs) resulted in larger tumors in SCID mice, while cells expressing shGLS1 actually resulted in smaller tumors compared to the control (shCont) (Fig. 5I). These data strongly support the likelihood that GLS2 exerts its antitumor effect through its ability to promote ferroptosis and this requires the GLS2 glutaminase core domain.

### Hepatocellular carcinomas down-regulate GLS2 levels which are correlated with the survival rates of HCC patients

To further address the physiological role of GLS2 in HCC and infer clinical relationships, we examined its expression profiles in livers of STAM mice that had developed HCC, which revealed that *Gls2* mRNA and protein levels were actually decreased at this stage (Fig. 6A and 6B). Reduced expression of *Gls2* was likely due to the hypermethylation of CpG islands in the *Gls2* promoter that we assessed, and which in turn likely resulted in the downregulation of *Gls2* expression in mouse HCC (Supplementary Fig. S10A and S10B). Immunohistological analysis demonstrated that *Gls2* protein levels were also decreased in the HCC samples compared to the non-HCC samples even though p53 levels themselves were increased in HCC (Fig. 6B and 6C). It is possible that the increased levels of p53 protein resulted from the combination of streptozotocin and high fat diet to which the mice were subjected.

In agreement with these results obtained from mice, examination of the Cancer Genome Atlas (TCGA) database revealed that the mRNA levels of both *GLS2* and the ferroptosis marker *PTGS2* are significantly lower in human HCC patients compared to normal patients, whereas *GLS1* mRNA levels are slightly higher in HCC, even though levels of p53 mRNA were similar between the two groups (Fig. 6D). To examine the relationship between GLS2 expression and clinical characteristics, we divided the patients into two groups based on the median of *GLS2* expression: i.e. a low group (below the median) and a high group (over the median). The group with low *GLS2* expression contains only HCC patients (Fig. 6E) and shows slight but significant reduction in *PTGS2* expression compared to the group of patients with high *GLS2* expression (Fig. 6F). Among patients with HCC, there was no

significant difference in age at initial pathological diagnosis between groups with low and high GLS2 levels (Fig. 6G). On the other hand, the G3 and G4 histological grades of HCC (where G1-G4 extend from lower to higher, respectively) were significantly higher in the group with low GLS2 (Fig. 6H). Importantly as well, Kaplan-Meier survival analysis using the KM-plotter database demonstrated that low expression levels of GLS2 are significantly correlated with poorer survival outcome in patients with not only HCC but also those with lung and breast cancers (Fig. 6I).

Further, using the cBioPortal Meta analysis tool, we performed cross-cancer analysis of *GLS2* gene for amplifications, deletions and mutations, which indicated that while a large number of tumor types mainly harbored amplifications, the deletions were also present in breast cancer and hepatobiliary cancer (Supplementary Fig. S11). Besides, using the catalogue of somatic mutations in cancer database (COSMIC) showed we determined that *GLS2* harbors relatively high rate of loss-of-function mutations (nonsense, inframe insertion, frameshift insertion, inframe deletion and frameshift deletion) in human hepatocellular carcinomas (Fig. 6J).

Taken together, these results indicate that GLS2 is downregulated in HCC and this is associated with increased histological malignancy and decreased survival.

## Discussion

In this study, we have used *Gls2* knockout mice and human cancer cells to evaluate the possibility that GLS2 is a suppressor of HCC, and that protection by GLS2 from such tumorigenesis involves its role in promoting ferroptosis. We show that *Gls2* KO mice have a marked propensity to develop late HCCs. Further, by subjecting mice to the STAM diet, ensuing HCC is exacerbated in the absence of GLS2. In concert with this and extending previous studies linking GLS2 to ferroptosis (24), hepatocytes from *Gls2* KO mice are more resistant to experimentally induced ferroptosis. In fact, not only cancer cells but also hepatocytes from mice display reduced ferroptosis when GLS2 is not expressed. These findings extend to human cancer cells derived from HCC where we demonstrate that modulation of GLS2 levels leads to correspondingly altered extents of ferroptosis. Most importantly, ferroptosis is required to suppress tumors derived from cells expressing wild-type GLS2 from forming in mice. Finally we show that human HCC cancer patients' tumors as well as HCCs from mice display reduced levels of GLS2. Taken together these data strongly support a role for GLS2 in ferroptosis and consequent tumor suppression.

Increased oxidative stress or involvement of ferroptosis has been previously postulated as a mechanism of hepatocellular carcinoma development in *Gls2* knockout mice (63–65), and our data indicate that ferroptosis may indeed be involved in preventing cancer onset and progression. Although Gao et al. (24) first reported that glutaminolysis and transferrin regulate ferroptosis, the mechanism has not been fully elucidated. We show here that of the two major glutaminases, GLS2 but not GLS1 can modulate ferroptosis. While there is only low homology between the N- and C-terminal regions of these two proteins, there is a high degree of homology in their respective glutaminase core domains, and we have found the GLS2 core domain to be necessary for the role of GLS2 in ferroptosis. A possible



explanation for this difference might be that GLS2 and GLS1 have different subcellular localizations; GLS2 is found in mitochondria while GLS1 is present in the cytoplasm (66). Interestingly, however, in previous reports (51), mitochondrial ROS does not increase during ferroptosis induction, even though mitochondria is the central organelle where significant amounts of cellular ROS are generated in response to stress.

As another explanation, the mitochondria might be important through contributing to the production of lipid peroxides or for the formation of microsomal membranes from membrane phospholipids that are involved in ferroptotic death. Several mitochondrial genes have been found to be associated with ferroptosis, and it is possible that peroxidation of cardiolipin, a mitochondria-specific phospholipid, links mitochondrial lipid peroxidation to ferroptosis (30, 67, 68). Conversely, there are also reports that the removal of mitochondrial DNA (51) or the removal of mitochondria itself (69) does not prevent ferroptosis. By way of reconciling these disparate roles, we speculate that since energy metabolic pathways are all interconnected, energy metabolism in mitochondria may be compensated in some contexts but not others.

We propose that in the context that we have studied, the primary role of mitochondria might be involved in the energy homeostasis that is associated with ferroptosis. In accordance with our hypothesis, a recent report provided evidence that TCA metabolites which are downstream of  $\alpha$ KG, such as succinate, fumarate and malate can cause the hyperpolarization of the mitochondrial membrane, which is associated with cysteine-deprivation-induced lipid ROS accumulation and ferroptosis (57). We suggest that GLS2 is involved in lipid ROS accumulation through  $\alpha$ KG-dependent activation of the TCA cycle and electron transport in mitochondria, where most ROS are produced and phospholipids are also abundant, and this is important for ferroptosis induction.

As GLS2 expression was reduced in HCC through hypermethylation of its promoter region, a chemical modulator of  $\alpha$ KG or glutaminolysis might have a strong therapeutic potential via ferroptosis induction for these cancers. This is in line with the finding that combining the ferroptosis inducer, erastin with chemotherapeutic drugs such as cytarabine/ara-C, cisplatin, doxorubicin/adriamycin, and temozolomide have shown a remarkable synergistic effect in anti-tumor activities (27).

In *Gls2* KO mice, the induction of ferroptosis was reduced in cells and tissues related to the liver that we studied and mice were afflicted primarily with HCC and lymphomas. But we do not know if other tissues were also defective in undergoing ferroptosis. As GLS2 is highly expressed in liver, this presents the possibility that there is a somewhat unique dependence on this protein for suppression of cancer through ferroptosis in this tissue.

However, while here we have mainly focused on hepatocellular carcinoma, other cancers that might potentially be suppressed due to ferroptosis, such as lymphoid tumors (53, 70–72) might also have a requirement for GLS2 in driving ferroptosis sensitivity. Further, while it is intriguing that *Gls2* KO mice develop liver cancer at a late age of 120 weeks, whether GLS2 can also be involved in other ferroptosis-associated diseases such as reperfusion injury and neuronal death (24, 73) is of considerable interest for future studies.

## Supplementary Material

Refer to Web version on PubMed Central for supplementary material.

## Acknowledgements

The authors are grateful to Yuko Yamagata, Erika Sugawara and Masanori Fujimoto of Chiba University as well as Ella Freulich at Columbia University for their technical assistance. The authors also want to thank Ichiro Tatsuno of Chiba Prefectural University of Health Sciences, Atsushi Kaneda of Chiba University and Satoshi Inoue of Saitama Medical University for his academic advice.

This research was supported by Grants-in-Aid for Scientific Research (C) 26430105 and 17K09875, International Joint Research Program #16KK0197, the Takeda Science Foundation, the Kowa Life Science Foundation, the Banyu Foundation, and the Kato Memorial Bioscience Foundation. This work was supported by JSPS KAKENHI Grant Number JP 16H06276 (AdAMS) as well as CA87497 to C.P. and B.S.

## References

1. Yang L, Venneti S, Nagrath D. Glutaminolysis: A Hallmark of Cancer Metabolism. *Annu Rev Biomed Eng.* 2017;19:163–94. [PubMed: 28301735]
2. Lamonte G, Tang X, Chen JL, Wu J, Ding CK, Keenan MM, et al. Acidosis induces reprogramming of cellular metabolism to mitigate oxidative stress. *Cancer Metab.* 2013;1(1):23. [PubMed: 24359630]
3. Araujo L, Khim P, Mkhikian H, Mortales CL, Demetriou M. Glycolysis and glutaminolysis cooperatively control T cell function by limiting metabolite supply to N-glycosylation. *Elife.* 2017;6.
4. Chung-Bok MI, Vincent N, Jhala U, Watford M. Rat hepatic glutaminase: identification of the full coding sequence and characterization of a functional promoter. *Biochem J.* 1997;324 ( Pt 1)(Pt 1):193–200. [PubMed: 9164856]
5. Gao P, Tchernyshyov I, Chang TC, Lee YS, Kita K, Ochi T, et al. c-Myc suppression of miR-23a/b enhances mitochondrial glutaminase expression and glutamine metabolism. *Nature.* 2009;458(7239):762–5. [PubMed: 19219026]
6. Wang JB, Erickson JW, Fuji R, Ramachandran S, Gao P, Dinavahi R, et al. Targeting mitochondrial glutaminase activity inhibits oncogenic transformation. *Cancer Cell.* 2010;18(3):207–19. [PubMed: 20832749]
7. Kahlert UD, Cheng M, Koch K, Marchionni L, Fan X, Raabe EH, et al. Alterations in cellular metabolome after pharmacological inhibition of Notch in glioblastoma cells. *Int J Cancer.* 2016;138(5):1246–55. [PubMed: 26422827]
8. Suzuki S, Tanaka T, Poyurovsky MV, Nagano H, Mayama T, Ohkubo S, et al. Phosphate-activated glutaminase (GLS2), a p53-inducible regulator of glutamine metabolism and reactive oxygen species. *Proc Natl Acad Sci U S A.* 2010;107(16):7461–6. [PubMed: 20351271]
9. Hu W, Zhang C, Wu R, Sun Y, Levine A, Feng Z. Glutaminase 2, a novel p53 target gene regulating energy metabolism and antioxidant function. *Proc Natl Acad Sci U S A.* 2010;107(16):7455–60. [PubMed: 20378837]
10. Luengo A, Gui DY, Vander Heiden MG. Targeting Metabolism for Cancer Therapy. *Cell Chem Biol.* 2017;24(9):1161–80. [PubMed: 28938091]
11. Gross MI, Demo SD, Dennison JB, Chen L, Chernov-Rogan T, Goyal B, et al. Antitumor activity of the glutaminase inhibitor CB-839 in triple-negative breast cancer. *Mol Cancer Ther.* 2014;13(4):890–901. [PubMed: 24523301]
12. Jacque N, Ronchetti AM, Larrue C, Meunier G, Birsén R, Willems L, et al. Targeting glutaminolysis has antileukemic activity in acute myeloid leukemia and synergizes with BCL-2 inhibition. *Blood.* 2015;126(11):1346–56. [PubMed: 26186940]
13. Choi YK, Park KG. Targeting Glutamine Metabolism for Cancer Treatment. *Biomol Ther (Seoul).* 2018;26(1):19–28. [PubMed: 29212303]

14. Sheikh TN, Patwardhan PP, Cremers S, Schwartz GK. Targeted inhibition of glutaminase as a potential new approach for the treatment of NF1 associated soft tissue malignancies. *Oncotarget*. 2017;8(55):94054–68.
15. Mates JM, Campos-Sandoval JA, de Los Santos-Jimenez J, Segura JA, Alonso FJ, Marquez J. Metabolic reprogramming of cancer by chemicals that target glutaminase isoenzymes. *Curr Med Chem*. 2019.
16. Le A, Lane AN, Hamaker M, Bose S, Gouw A, Barbi J, et al. Glucose-independent glutamine metabolism via TCA cycling for proliferation and survival in B cells. *Cell Metab*. 2012;15(1):110–21. [PubMed: 22225880]
17. Lobo C, Ruiz-Bellido MA, Aledo JC, Marquez J, Nunez De Castro I, Alonso FJ. Inhibition of glutaminase expression by antisense mRNA decreases growth and tumourigenicity of tumour cells. *Biochem J*. 2000;348 Pt 2:257–61. [PubMed: 10816417]
18. Zhang C, Liu J, Zhao Y, Yue X, Zhu Y, Wang X, et al. Glutaminase 2 is a novel negative regulator of small GTPase Rac1 and mediates p53 function in suppressing metastasis. *Elife*. 2016;5:e10727.
19. Liu J, Zhang C, Lin M, Zhu W, Liang Y, Hong X, et al. Glutaminase 2 negatively regulates the PI3K/AKT signaling and shows tumor suppression activity in human hepatocellular carcinoma. *Oncotarget*. 2014;5(9):2635–47. [PubMed: 24797434]
20. Szeliga M, Zgrzywa A, Obara-Michlewska M, Albrecht J. Transfection of a human glioblastoma cell line with liver-type glutaminase (LGA) down-regulates the expression of DNA-repair gene MGMT and sensitizes the cells to alkylating agents. *J Neurochem*. 2012;123(3):428–36. [PubMed: 22888977]
21. Martin-Rufian M, Nascimento-Gomes R, Higuero A, Crisma AR, Campos-Sandoval JA, Gomez-Garcia MC, et al. Both GLS silencing and GLS2 overexpression synergize with oxidative stress against proliferation of glioma cells. *J Mol Med (Berl)*. 2014;92(3):277–90. [PubMed: 24276018]
22. Lee YZ, Yang CW, Chang HY, Hsu HY, Chen IS, Chang HS, et al. Discovery of selective inhibitors of Glutaminase-2, which inhibit mTORC1, activate autophagy and inhibit proliferation in cancer cells. *Oncotarget*. 2014;5(15):6087–101. [PubMed: 25026281]
23. Xiang L, Xie G, Liu C, Zhou J, Chen J, Yu S, et al. Knock-down of glutaminase 2 expression decreases glutathione, NADH, and sensitizes cervical cancer to ionizing radiation. *Biochim Biophys Acta*. 2013;1833(12):2996–3005. [PubMed: 23954443]
24. Gao M, Monian P, Quadri N, Ramasamy R, Jiang X. Glutaminolysis and Transferrin Regulate Ferroptosis. *Mol Cell*. 2015;59(2):298–308. [PubMed: 26166707]
25. Shen Z, Song J, Yung BC, Zhou Z, Wu A, Chen X. Emerging Strategies of Cancer Therapy Based on Ferroptosis. *Adv Mater*. 2018;30(12):e1704007.
26. Lu B, Chen XB, Ying MD, He QJ, Cao J, Yang B. The Role of Ferroptosis in Cancer Development and Treatment Response. *Front Pharmacol*. 2017;8:992. [PubMed: 29375387]
27. Mou Y, Wang J, Wu J, He D, Zhang C, Duan C, et al. Ferroptosis, a new form of cell death: opportunities and challenges in cancer. *J Hematol Oncol*. 2019;12(1):34. [PubMed: 30925886]
28. Jennis M, Kung CP, Basu S, Budina-Kolomets A, Leu JI, Khaku S, et al. An African-specific polymorphism in the TP53 gene impairs p53 tumor suppressor function in a mouse model. *Genes Dev*. 2016;30(8):918–30. [PubMed: 27034505]
29. Yang WS, Stockwell BR. Ferroptosis: Death by Lipid Peroxidation. *Trends Cell Biol*. 2016;26(3):165–76. [PubMed: 26653790]
30. Xie Y, Hou W, Song X, Yu Y, Huang J, Sun X, et al. Ferroptosis: process and function. *Cell Death Differ*. 2016;23(3):369–79. [PubMed: 26794443]
31. Skarnes WC, Rosen B, West AP, Koutsourakis M, Bushell W, Iyer V, et al. A conditional knockout resource for the genome-wide study of mouse gene function. *Nature*. 2011;474(7351):337–42. [PubMed: 21677750]
32. Venkatesh D, O'Brien NA, Zandkarimi F, Tong DR, Stokes ME, Dunn DE, et al. MDM2 and MDMX promote ferroptosis by PPAR $\alpha$ -mediated lipid remodeling. *Genes Dev*. 2020;34(7–8):526–43. [PubMed: 32079652]
33. Larraufie MH, Yang WS, Jiang E, Thomas AG, Slusher BS, Stockwell BR. Incorporation of metabolically stable ketones into a small molecule probe to increase potency and water solubility. *Bioorg Med Chem Lett*. 2015;25(21):4787–92. [PubMed: 26231156]

34. Honda A, Hirose M, Hatori M, Matoba S, Miyoshi H, Inoue K, et al. Generation of induced pluripotent stem cells in rabbits: potential experimental models for human regenerative medicine. *J Biol Chem*. 2010;285(41):31362–9. [PubMed: 20670936]
35. Hirayama T. Fluorescent probes for the detection of catalytic Fe(II) ion. *Free Radic Biol Med*. 2019;133:38–45. [PubMed: 29990536]
36. Kanai A, Suzuki K, Tanimoto K, Mizushima-Sugano J, Suzuki Y, Sugano S. Characterization of STAT6 target genes in human B cells and lung epithelial cells. *DNA Res*. 2011;18(5):379–92. [PubMed: 21828071]
37. Mortazavi A, Williams BA, McCue K, Schaeffer L, Wold B. Mapping and quantifying mammalian transcriptomes by RNA-Seq. *Nat Methods*. 2008;5(7):621–8. [PubMed: 18516045]
38. Miki T, Nagashima K, Tashiro F, Kotake K, Yoshitomi H, Tamamoto A, et al. Defective insulin secretion and enhanced insulin action in KATP channel-deficient mice. *Proc Natl Acad Sci U S A*. 1998;95(18):10402–6.
39. Yoshimoto S, Loo TM, Atarashi K, Kanda H, Sato S, Oyadomari S, et al. Obesity-induced gut microbial metabolite promotes liver cancer through senescence secretome. *Nature*. 2013;499(7456):97–101. [PubMed: 23803760]
40. Chen Y. Scratch Wound Healing Assay. *Bio-protocol*. 2012;2(5):e100.
41. Loo TM, Kamachi F, Watanabe Y, Yoshimoto S, Kanda H, Arai Y, et al. Gut Microbiota Promotes Obesity-Associated Liver Cancer through PGE2-Mediated Suppression of Antitumor Immunity. *Cancer Discov*. 2017.
42. Tokunaga Y, Osawa Y, Ohtsuki T, Hayashi Y, Yamaji K, Yamane D, et al. Selective inhibitor of Wnt/beta-catenin/CBP signaling ameliorates hepatitis C virus-induced liver fibrosis in mouse model. *Sci Rep*. 2017;7(1):325. [PubMed: 28336942]
43. Sakuma I, Higuchi S, Fujimoto M, Takiguchi T, Nakayama A, Tamura A, et al. Cushing Syndrome Due to ACTH-Secreting Pheochromocytoma, Aggravated by Glucocorticoid-Driven Positive-Feedback Loop. *J Clin Endocrinol Metab*. 2016;101(3):841–6. [PubMed: 26700559]
44. Fujii M, Shibasaki Y, Wakamatsu K, Honda Y, Kawauchi Y, Suzuki K, et al. A murine model for non-alcoholic steatohepatitis showing evidence of association between diabetes and hepatocellular carcinoma. *Med Mol Morphol*. 2013;46(3):141–52. [PubMed: 23430399]
45. Siveski-Iliskovic N, Kaul N, Singal PK. Probuco promotes endogenous antioxidants and provides protection against adriamycin-induced cardiomyopathy in rats. *Circulation*. 1994;89(6):2829–35. [PubMed: 8205698]
46. Zhang X, Li Z, Liu X, Xu X, Shen W, Mei Z. Effects of probucol on hepatic tumor necrosis factor-alpha, interleukin-6 and adiponectin receptor-2 expression in diabetic rats. *J Gastroenterol Hepatol*. 2009;24(6):1058–63. [PubMed: 19220660]
47. Merat S, Malekzadeh R, Sohrabi MR, Hormazdi M, Naserimoghadam S, Mikaeli J, et al. Probuco in the treatment of nonalcoholic steatohepatitis: an open-labeled study. *J Clin Gastroenterol*. 2003;36(3):266–8. [PubMed: 12590240]
48. Stockwell BR, Friedmann Angeli JP, Bayir H, Bush AI, Conrad M, Dixon SJ, et al. Ferroptosis: A Regulated Cell Death Nexus Linking Metabolism, Redox Biology, and Disease. *Cell*. 2017;171(2):273–85. [PubMed: 28985560]
49. Hirschhorn T, Stockwell BR. The development of the concept of ferroptosis. *Free Radic Biol Med*. 2019;133:130–43. [PubMed: 30268886]
50. Bueno DC, Canto RFS, de Souza V, Andregueti RR, Barbosa FAR, Naime AA, et al. New Probuco Analogues Inhibit Ferroptosis, Improve Mitochondrial Parameters, and Induce Glutathione Peroxidase in HT22 Cells. *Mol Neurobiol*. 2020;57(8):3273–90. [PubMed: 32514861]
51. Dixon SJ, Lemberg KM, Lamprecht MR, Skouta R, Zaitsev EM, Gleason CE, et al. Ferroptosis: an iron-dependent form of nonapoptotic cell death. *Cell*. 2012;149(5):1060–72. [PubMed: 22632970]
52. Dixon SJ, Patel DN, Welsch M, Skouta R, Lee ED, Hayano M, et al. Pharmacological inhibition of cystine-glutamate exchange induces endoplasmic reticulum stress and ferroptosis. *Elife*. 2014;3:e02523.
53. Yang WS, SriRamaratnam R, Welsch ME, Shimada K, Skouta R, Viswanathan VS, et al. Regulation of ferroptotic cancer cell death by GPX4. *Cell*. 2014;156(1–2):317–31. [PubMed: 24439385]

54. Gao M, Monian P, Pan Q, Zhang W, Xiang J, Jiang X. Ferroptosis is an autophagic cell death process. *Cell Res.* 2016;26(9):1021–32. [PubMed: 27514700]
55. Liu J, Kuang F, Kroemer G, Klionsky DJ, Kang R, Tang D. Autophagy-Dependent Ferroptosis: Machinery and Regulation. *Cell Chem Biol.* 2020;27(4):420–35. [PubMed: 32160513]
56. Drummen GP, van Liebergen LC, Op den Kamp JA, Post JA. C11-BODIPY(581/591), an oxidation-sensitive fluorescent lipid peroxidation probe: (micro)spectroscopic characterization and validation of methodology. *Free Radic Biol Med.* 2002;33(4):473–90. [PubMed: 12160930]
57. Gao M, Yi J, Zhu J, Minikes AM, Monian P, Thompson CB, et al. Role of Mitochondria in Ferroptosis. *Mol Cell.* 2019;73(2):354–63.e3. [PubMed: 30581146]
58. Moon SH, Huang CH, Houlihan SL, Regunath K, Freed-Pastor WA, Morris JPt, et al. p53 Represses the Mevalonate Pathway to Mediate Tumor Suppression. *Cell.* 2019;176(3):564–80.e19. [PubMed: 30580964]
59. Jiang L, Kon N, Li T, Wang SJ, Su T, Hibshoosh H, et al. Ferroptosis as a p53-mediated activity during tumour suppression. *Nature.* 2015;520(7545):57–62. [PubMed: 25799988]
60. Wang SJ, Li D, Ou Y, Jiang L, Chen Y, Zhao Y, et al. Acetylation Is Crucial for p53-Mediated Ferroptosis and Tumor Suppression. *Cell Rep.* 2016;17(2):366–73. [PubMed: 27705786]
61. Murphy ME. Ironing out how p53 regulates ferroptosis. *Proc Natl Acad Sci U S A.* 2016;113(44):12350–2. [PubMed: 27791175]
62. Zhang K, Wu L, Zhang P, Luo M, Du J, Gao T, et al. miR-9 regulates ferroptosis by targeting glutamic-oxaloacetic transaminase GOT1 in melanoma. *Mol Carcinog.* 2018;57(11):1566–76. [PubMed: 30035324]
63. Nie J, Lin B, Zhou M, Wu L, Zheng T. Role of ferroptosis in hepatocellular carcinoma. *J Cancer Res Clin Oncol.* 2018;144(12):2329–37. [PubMed: 30167889]
64. Xia X, Fan X, Zhao M, Zhu P. The Relationship between Ferroptosis and Tumors: A Novel Landscape for Therapeutic Approach. *Curr Gene Ther.* 2019;19(2):117–24. [PubMed: 31264548]
65. Yu H, Guo P, Xie X, Wang Y, Chen G. Ferroptosis, a new form of cell death, and its relationships with tumorous diseases. *J Cell Mol Med.* 2017;21(4):648–57. [PubMed: 27860262]
66. Cassago A, Ferreira AP, Ferreira IM, Fornezari C, Gomes ER, Greene KS, et al. Mitochondrial localization and structure-based phosphate activation mechanism of Glutaminase C with implications for cancer metabolism. *Proc Natl Acad Sci U S A.* 2012;109(4):1092–7. [PubMed: 22228304]
67. Krainz T, Gaschler MM, Lim C, Sacher JR, Stockwell BR, Wipf P. A Mitochondrial-Targeted Nitroxide Is a Potent Inhibitor of Ferroptosis. *ACS Cent Sci.* 2016;2(9):653–9. [PubMed: 27725964]
68. Ji J, Baart S, Vikulina AS, Clark RS, Anthonymuthu TS, Tyurin VA, et al. Deciphering of mitochondrial cardiolipin oxidative signaling in cerebral ischemia-reperfusion. *J Cereb Blood Flow Metab.* 2015;35(2):319–28. [PubMed: 25407268]
69. Gaschler MM, Hu F, Feng H, Linkermann A, Min W, Stockwell BR. Determination of the Subcellular Localization and Mechanism of Action of Ferrostatins in Suppressing Ferroptosis. *ACS Chem Biol.* 2018;13(4):1013–20. [PubMed: 29512999]
70. Iglehart JK, York RM, Modest AP, Lazarus H, Livingston DM. Cystine requirement of continuous human lymphoid cell lines of normal and leukemic origin. *J Biol Chem.* 1977;252(20):7184–91. [PubMed: 903356]
71. Gout PW, Buckley AR, Simms CR, Bruchofsky N. Sulfasalazine, a potent suppressor of lymphoma growth by inhibition of the x(c)- cystine transporter: a new action for an old drug. *Leukemia.* 2001;15(10):1633–40. [PubMed: 11587223]
72. Gout PW, Simms CR, Robertson MC. In vitro studies on the lymphoma growth-inhibitory activity of sulfasalazine. *Anticancer Drugs.* 2003;14(1):21–9. [PubMed: 12544255]
73. Do Van B, Gouel F, Jonneaux A, Timmerman K, Gele P, Petrault M, et al. Ferroptosis, a newly characterized form of cell death in Parkinson's disease that is regulated by PKC. *Neurobiol Dis.* 2016;94:169–78. [PubMed: 27189756]

### Significance

This study demonstrates that the key regulator of glutaminolysis, GLS2, can limit hepatocellular carcinoma *in vivo* by promoting ferroptosis through  $\alpha$ -ketoglutarate dependent lipid ROS, which in turn might lay the foundation for a novel therapeutic approach.



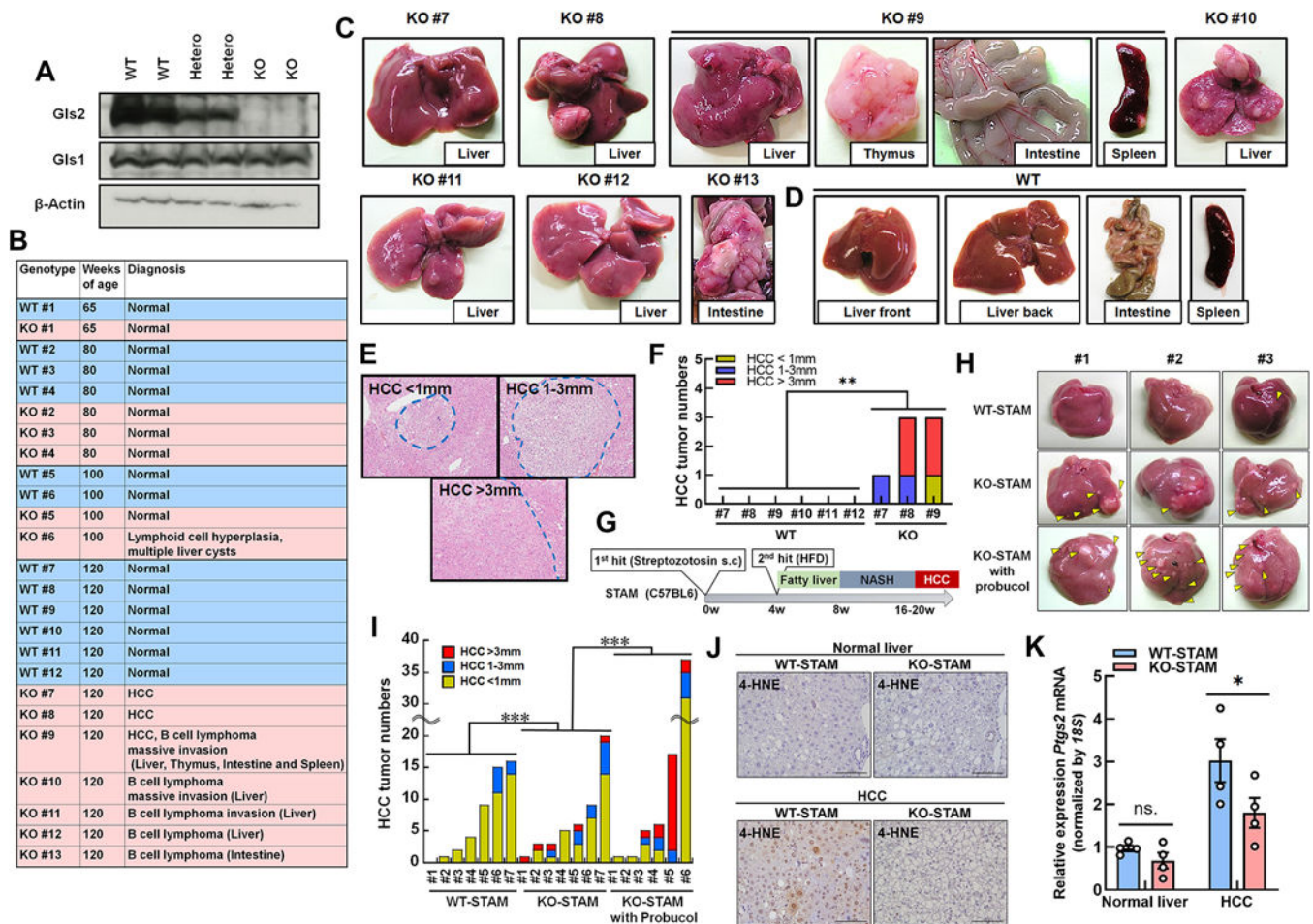


**Figure 1. Progression of tumorigenesis in the absence of Gls2**

**A**, Immunoblot showing Gls2 and Gls1 protein levels in the livers of knockout (KO; Gls2<sup>-/-</sup>), heterozygous (Hetero; Gls2<sup>+/-</sup>), and wild-type (WT; Gls2<sup>+/+</sup>) mice. Actin is the loading control. **B**, Summary of tumorigenesis in WT and KO mice after 65 weeks of age. HCC signifies hepatocellular carcinoma. **C-D**, Macroscopic findings of tumorigenesis at 120 weeks of age in **(C)** KO mice and **(D)** in WT mice. **E**, H&E stain of liver sections indicating HCC < 1 mm, HCC 1 mm–3 mm, and HCC >3 mm. HCC; Hepatocellular carcinoma. **F**, The average number of liver tumors and the relative size distribution of HCC in two KO mice at 120 weeks was determined based on the analysis of the H&E stain (classified as >3 mm, 1 mm–3 mm, < 3 mm) shown in **E**. \*\**p* < 0.01. **G**, Diagram showing generation and pathological analysis of Stelic Animal Model (STAM), a model for non-alcoholic steatohepatitis (NASH) and HCC. **H**, Macroscopic findings of tumorigenesis in the three experimental groups of STAM: WT mice (WT-STAM), KO mice (KO-STAM) and KO mice fed with high-fat diets mixed with 1% probucol (KO-STAM with probucol). The arrowheads indicate HCCs. **I**, The average number of tumors and the relative size distribution of HCC from the liver of WT-STAM, KO-STAM, and KO-STAM with probucol at 15 weeks of age were determined based on the analysis of H&E staining (classified as < 1 mm, 1 mm–3 mm, >3 mm). \*\*\**p* < 0.001. **J**, The immunohistochemical appearance of 4-HNE (brown) in normal liver and HCCs of WT-STAM and KO-STAM. Scale bars;

100  $\mu\text{m}$ . **K**, Expression levels of Ptg2 (mRNA) in normal liver and HCCs of WT-STAM and KO-STAM were determined by the comparative threshold cycle method and then normalized to 18S expression. Values are the means  $\pm$  SEM. \* $p < 0.05$ .

Author Manuscript

Author Manuscript

Author Manuscript

Author Manuscript

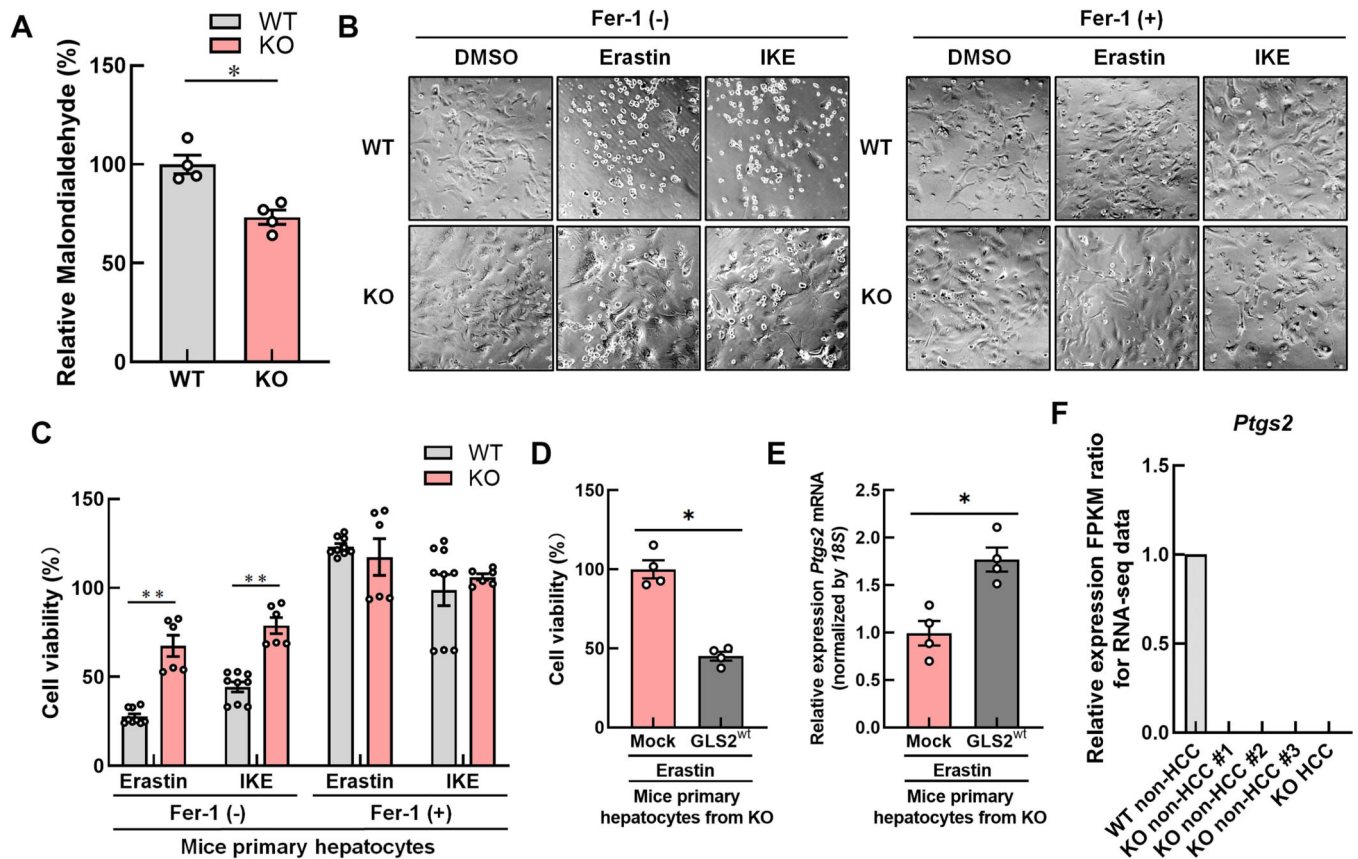


**Figure 2. Loss of Gls2 results in HCC lesions with increased resistance to ferroptosis**

**A**, The levels of malondialdehyde (MDA), the end product of lipid peroxidation, in the livers from KO (22 weeks, n=4) and WT (22 weeks, n=4) mice. Values are the means  $\pm$  SEM. \*P < 0.05. **B-C**, Primary hepatocytes from WT (20 weeks, n=9) or KO mice (20 weeks, n=6) were treated with indicated ferroptosis inducers (erastin 20  $\mu$ M and IKE 10  $\mu$ M) for 72 hours in the absence or presence of the ferroptosis inhibitor ferrostatin-1 (Fer-1 20  $\mu$ M). Representative visualization of the treated primary hepatocytes from WT and KO mice are shown in **(B)** (20x magnification). ATP based cell viability was assayed post these treatments and the corresponding data in **(C)** are presented as a percentage of the control (DMSO). Values are the means  $\pm$  SEM. \*\*p < 0.01. **D-E**, Cell viability in **(D)** and *Ptgs2* gene expression in **(E)** were assayed in mice primary hepatocytes from KO mice (20 weeks) transfected with p3 $\times$ FLAG-CMV10-empty vector (Mock, n=4) or p3 $\times$ FLAG-CMV10-hGLS2 vector (GLS2<sup>wt</sup>, n=4). **F**, RNA levels of the ferroptosis marker, *Ptgs2* were obtained from RNA-sequencing analysis performed in liver tissues of WT with non-HCC (20 weeks, n=1), KO with non-HCC (20 weeks, n=3) and KO with HCC (120 weeks, n=1).

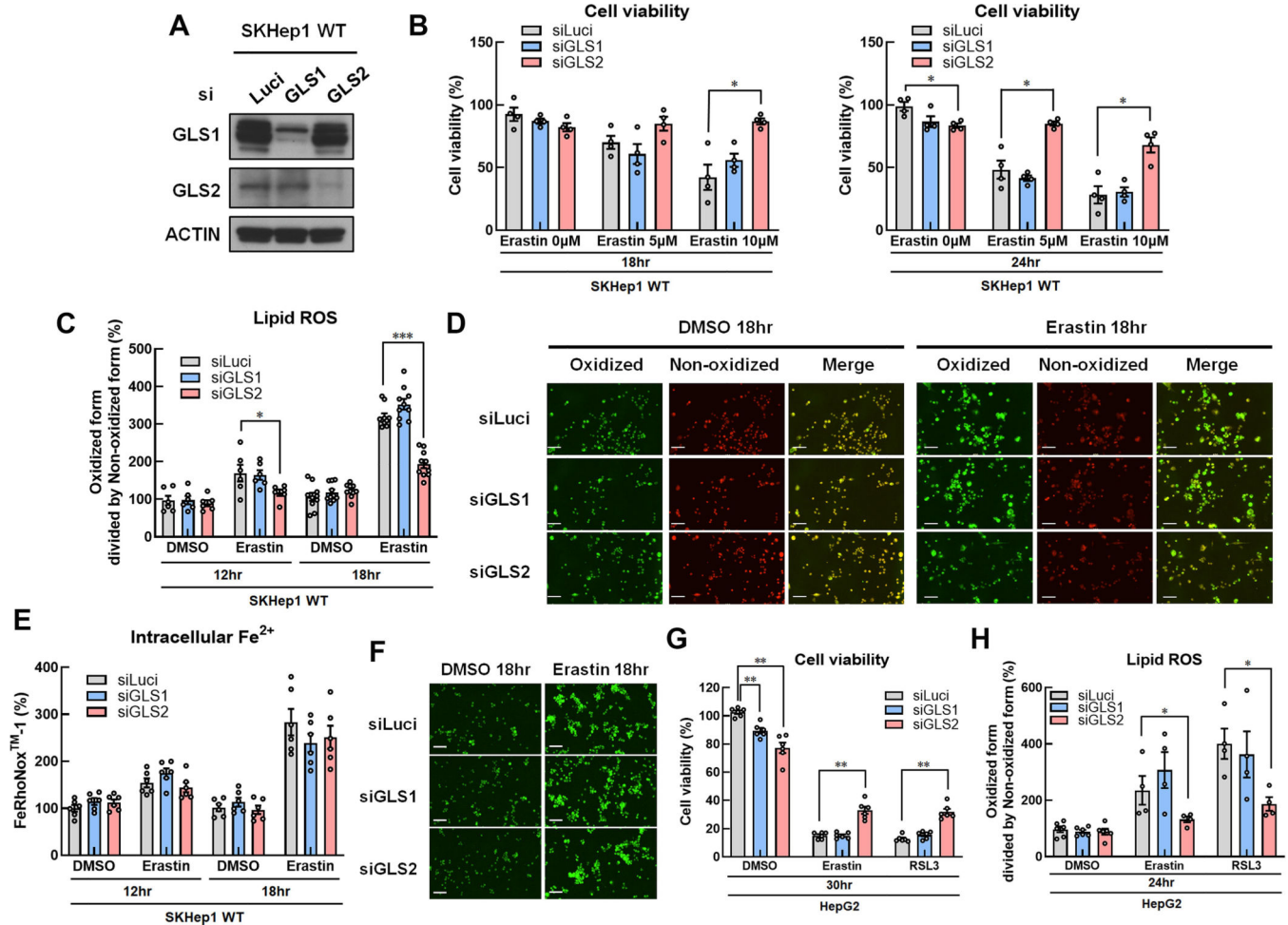


**Figure 3. GLS2 promotes an increase in lipid ROS and a concomitant increase in death due to erastin treatment**

**A**, SKHeP1 WT cells were transfected with luciferase RNAi (siLuci), hGLS1 RNAi (siGLS1), or hGLS2 RNAi (siGLS2) for 48 hours followed by immunoblot analysis to detect GLS1 and GLS2 or actin as indicated. **B**, Cell viability of SKHeP1 WT cells that were transfected with siLuci, siGLS1, or siGLS2 for 36 hours and then treated with erastin (0, 5, or 10  $\mu$ M). The viability was assayed at 18 hours (left panel) and 24 hours (right panel) post erastin treatment. Values are the means  $\pm$  SEM (n=4). \*p < 0.05 versus siLuci. **C-D**, SKHeP1 WT cells were transfected with siLuci, siGLS1, or siGLS2 for 36 hours and then treated with vehicle (DMSO) or erastin (5  $\mu$ M) for 12 hours (n=6) or 18 hours (n=10). Lipid ROS was detected by C11-BODIPY: the ratio of oxidized form (green) to the non-oxidized form (red) are presented. Bar graph in (C) depicts means  $\pm$  SEM. \*\*\*p < 0.001, \*p < 0.05 versus siLuci. Representative images are shown in (D). **E-F**, Intracellular  $Fe^{2+}$  was detected by FeRhoNox<sup>TM</sup>-1 a fluorescent probe that measures labile iron. The green fluorescence signal from the probe is shown in representative images in F. The bar graph in E depicts means  $\pm$  SEM (n=6). Scale bars in (D) and (F) 100  $\mu$ m. **G-H**, Cell viability in (G) and Lipid ROS in (H) were measured in HepG2 cells that were transfected with siLuci, siGLS1, or siGLS2 for 36 hours and then treated with vehicle (DMSO), erastin (10  $\mu$ M) or RSL3 (3

$\mu\text{M}$ ). The cells were treated for 30 hours (n=6) in **(G)** and for 24 hours (n=4–6) in **(H)**. Bar graphs depict means  $\pm$  SEM., \*\*p < 0.01, \*p < 0.05 versus siLuci.

Author Manuscript

Author Manuscript

Author Manuscript

Author Manuscript



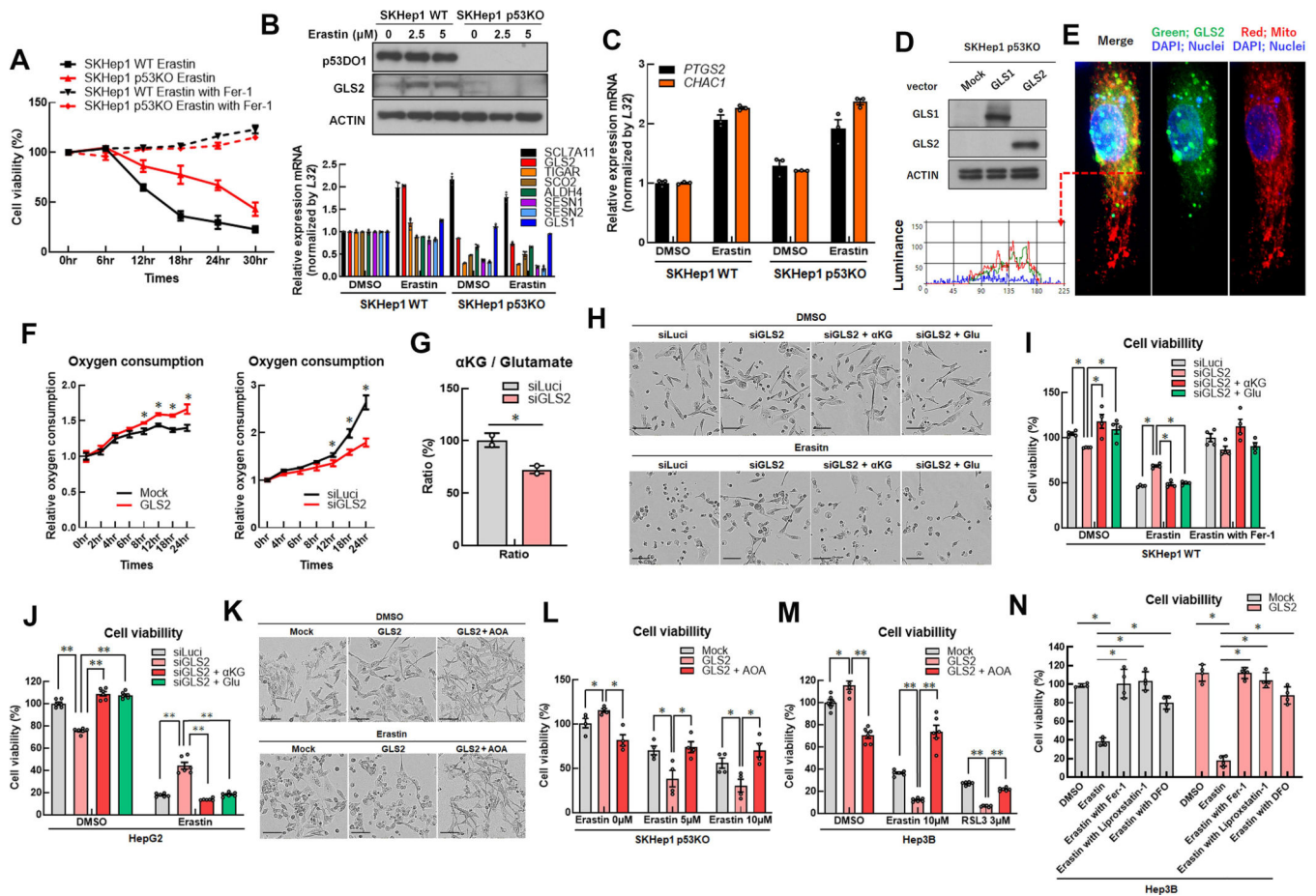


**Figure 4. GLS2 mediates ferroptosis sensitivity via α-ketoglutarate (αKG)**

**A**, Cell viability in SKHep1 WT cells or SKHep1 p53 knockout cells (SKHep1 p53KO cells) in response to treatment with erastin (5 μM) in the presence or absence of ferrostatin 1 (Fer-1; 5 μM) was measured at the indicated time points. Values are the means ± SEM (n=4). **B**, Immunoblot analysis of p53 and GLS2 expression in SKHep1 WT or SKHep1 p53KO cells following treatment with erastin (0, 2.5 or 5 μM) for 12 hours (upper panel). Change in mRNA levels of the indicated p53 target genes along with *GLS1* after DMSO or erastin (5 μM) treatment for 12 hours in SKHep1 WT or SKHep1 p53KO cells (lower panel). **C**, Change in mRNA levels of ferroptosis markers after DMSO or erastin (5 μM) treatment for 12 hours in SKHep1 WT or SKHep1 p53KO cells. **D**, SKHep1 p53KO cells were transfected with p3×FLAG-CMV10-empty vector (Mock), p3×FLAG-CMV10-hGLS1 (GLS1) or p3×FLAG-CMV10-hGLS2 (GLS2) constructs for 48 hours prior to lysis and processing for immunoblotting with anti-GLS2 antibody. **E**, Intracellular colocalization of GLS2 (PacGFPN1-hGLS2) and mitochondria (Mito tracker) in SKHep1 KO cells. **F**, Relative oxygen consumption rate in SKHep1 p53KO cells transfected with Mock or GLS2 (left panel). Relative oxygen consumption rate in SKHep1 WT cells transfected with luciferase RNAi (siLuci) (left) or hGLS2 RNAi (siGLS2) (right). \*p < 0.05 versus Mock or siLuci at each time point. **G**, Intracellular metabolite levels were quantified by CE-MS analysis and normalized to the number of SKHep1 WT cells. Then ratios of α-ketoglutarate (αKG) to glutamate in SKHep1 WT cells transfected with siLuci (gray)



or siGLS2 (red) (for 48 hours) were calculated. **H-I**, SKHep1 WT cells were transfected with either control (siLuci) or siGLS2 for 36 hours and then treated with erastin (5  $\mu$ M) for 18 hours.  $\alpha$ -ketoglutarate ( $\alpha$ KG 10 mM) or glutamate (Glu 500  $\mu$ M) was added to culture medium at the same time as erastin and then cell morphology (**H**) and viability (**I**) were determined. Bar graph in (**I**) depicts means  $\pm$  SEM (n=4). \*p < 0.05 versus siGLS2. **J**, Cell viability of HepG2 cells that were transfected with either control (siLuci) or siGLS2 for 36 hours and then treated with erastin (10  $\mu$ M) for 30 hours.  $\alpha$ -ketoglutarate ( $\alpha$ KG 10 mM) or glutamate (Glu 500  $\mu$ M) was added to culture medium at the same time as erastin. Bar graph in J depicts means  $\pm$  SEM (n=6). \*\*p < 0.01 versus siGLS2. **K-L**, SK Hep1 p53KO cells were transfected with Mock or GLS2 constructs for 24 hours and then cells were treated with DMSO, erastin (5  $\mu$ M or 10  $\mu$ M) alone, or erastin (5  $\mu$ M or 10  $\mu$ M) with AOA (5 mM) for 24 hours. Cell morphology (**K**) and cell viability (**L**) were assayed for these treated cells. Scale bar: 100  $\mu$ m (in H and K). Bar graph in L depicts means  $\pm$  SEM (n=4). \*p < 0.05 versus GLS2. **M-N**, Cell viability of Hep3B cells that were transfected with Mock or GLS2 constructs for 24 hours and then cells were treated for 24 hours with either (**M**) DMSO or ferroptosis inducers (erastin 10  $\mu$ M or RSL3 3  $\mu$ M) or indicated ferroptosis inducer with AOA (10 mM) or (**N**) erastin (10  $\mu$ M) in the absence or presence of the ferroptosis inhibitor (Fer-1 10  $\mu$ M, Liproxstatin 2  $\mu$ M or DFO 50  $\mu$ M). Bar graphs in (**M**) and (**N**) depict means  $\pm$  SEM (n=6). \*\*p < 0.01, \*p < 0.05 - versus GLS2 for (**M**) or versus erastin in (**N**).

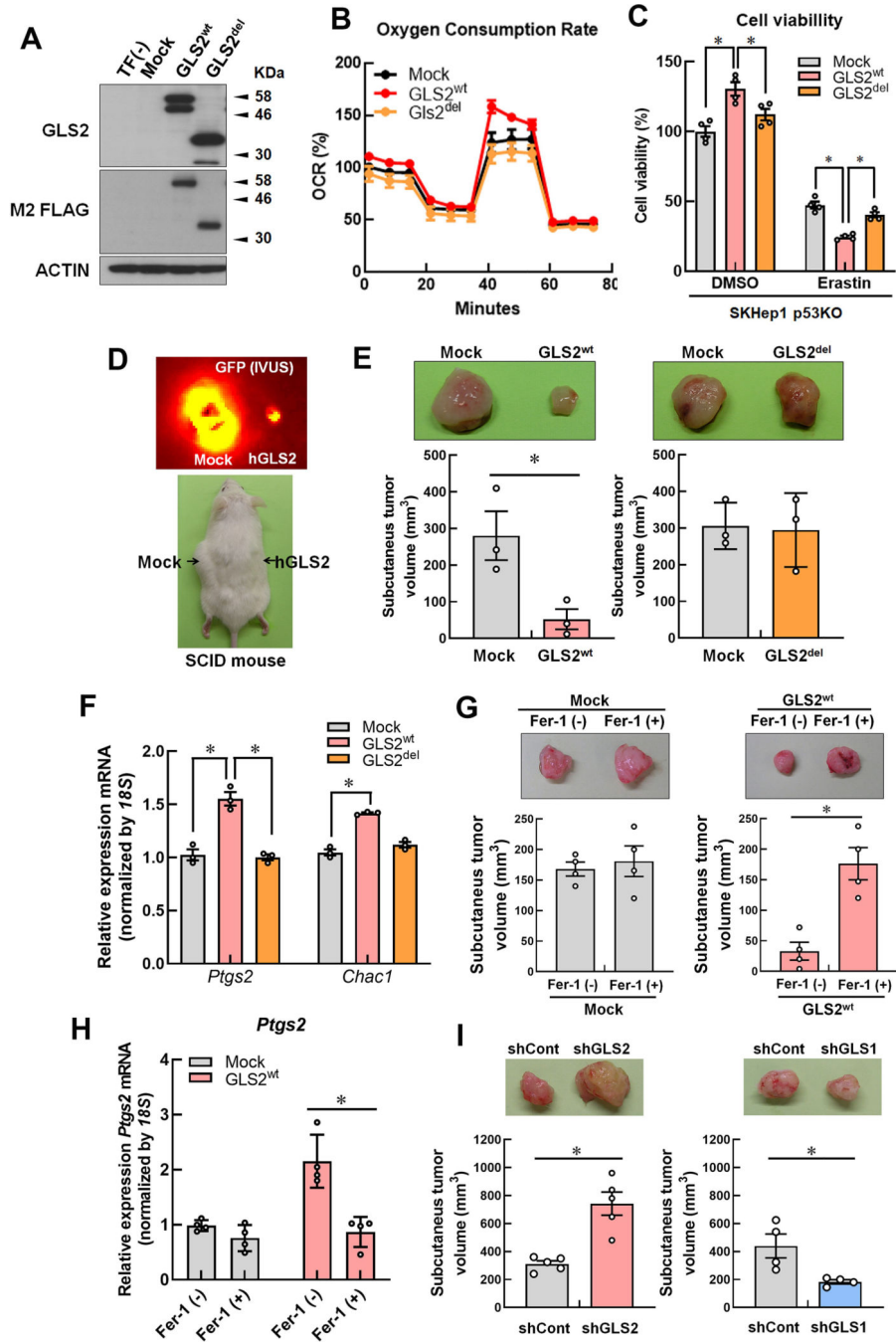


**Figure 5. GLS2 requires its core domain to promote ferroptosis and tumor suppression**

**A**, Western blot analysis of GLS2 expression in SKHep1 p53KO cells transfected with p3×FLAG-CMV10-empty vector (Mock) or p3×FLAG-CMV10-hGLS2 vector (GLS2<sup>wt</sup>) or p3×FLAG-CMV10-hGLS2 177–463 deletion mutant vector (GLS2<sup>del</sup>). **B**, SKHep1 p53KO cells were transfected with Mock, GLS2<sup>wt</sup>, or GLS2<sup>del</sup> constructs for 48 hours and then oxygen consumption rate (OCR) as recorded using a flux analyzer. The OCR was measured at baseline and after treatment with oligomycin, FCCP, and a mixture of antimycin and rotenone. **C**, SKHep1 p53KO cells were transfected with Mock, GLS2<sup>wt</sup>

or GLS2<sup>del</sup> constructs for 24 hours and then treated with erastin (5  $\mu$ M) for 24 hours to assay changes in cell viability. Bar graph depicts means  $\pm$  SEM (n=4). \*p < 0.05 versus GLS2<sup>wt</sup>. **D**, Xenograft tumors were obtained by subcutaneously injecting SKHep1 p53 KO cells that were transfected with either the GLS2<sup>wt</sup> lentivirus vector or CSII-EF-RfA-IRES2-Venus-empty vector (Mock) into SCID mice. Injections of indicated lentiviral vectors were performed on the right and left flanks of the same SCID mice. GFP expressed by the indicated lentivirus vectors was measured using the IVIS imaging system. **E**, Top panel- Representative macroscopic findings of the results of the procedure shown in **(D)**. Bottom panel- Volume of subcutaneous tumors obtained 6 weeks after injection of SKHep1 p53KO cells treated with Mock lentivirus vector on the left flank and either GLS2<sup>wt</sup> (left panel) or hGLS2<sup>del</sup> (right panel) on the right flank in SCID mice (n=3). **F**, RT-qPCR analysis of ferroptosis markers, *Ptgs2* and *Chac1* expression in subcutaneous tumors shown in **(E)**. **G**, Representative macroscopic findings and volume measurements of subcutaneous tumors in SCID mice (n=4) that were obtained 6 weeks after injection of SKHep1 p53 KO cells treated with left panel- GLS2<sup>wt</sup> (left flank) and GLS2<sup>wt</sup> with ferroptosis inhibitor Fer-1 (right flank) and right panel- Mock lentivirus vector (left flank) and Mock with Fer-1 (right flank). **H**, RT-qPCR analysis of ferroptosis marker, *Ptgs2* expression in subcutaneous tumors shown in **(G)**. **I**, Representative macroscopic findings and volume measurements of subcutaneous tumors obtained 6 weeks after injection of SKHep1 cells treated with shGLS2 or shGLS1 (right flank; n = 4) and shCont lentivirus vector (left flank; n = 5). Bar graph in **C, E-I** depicts means  $\pm$  SEM. \*p < 0.05.

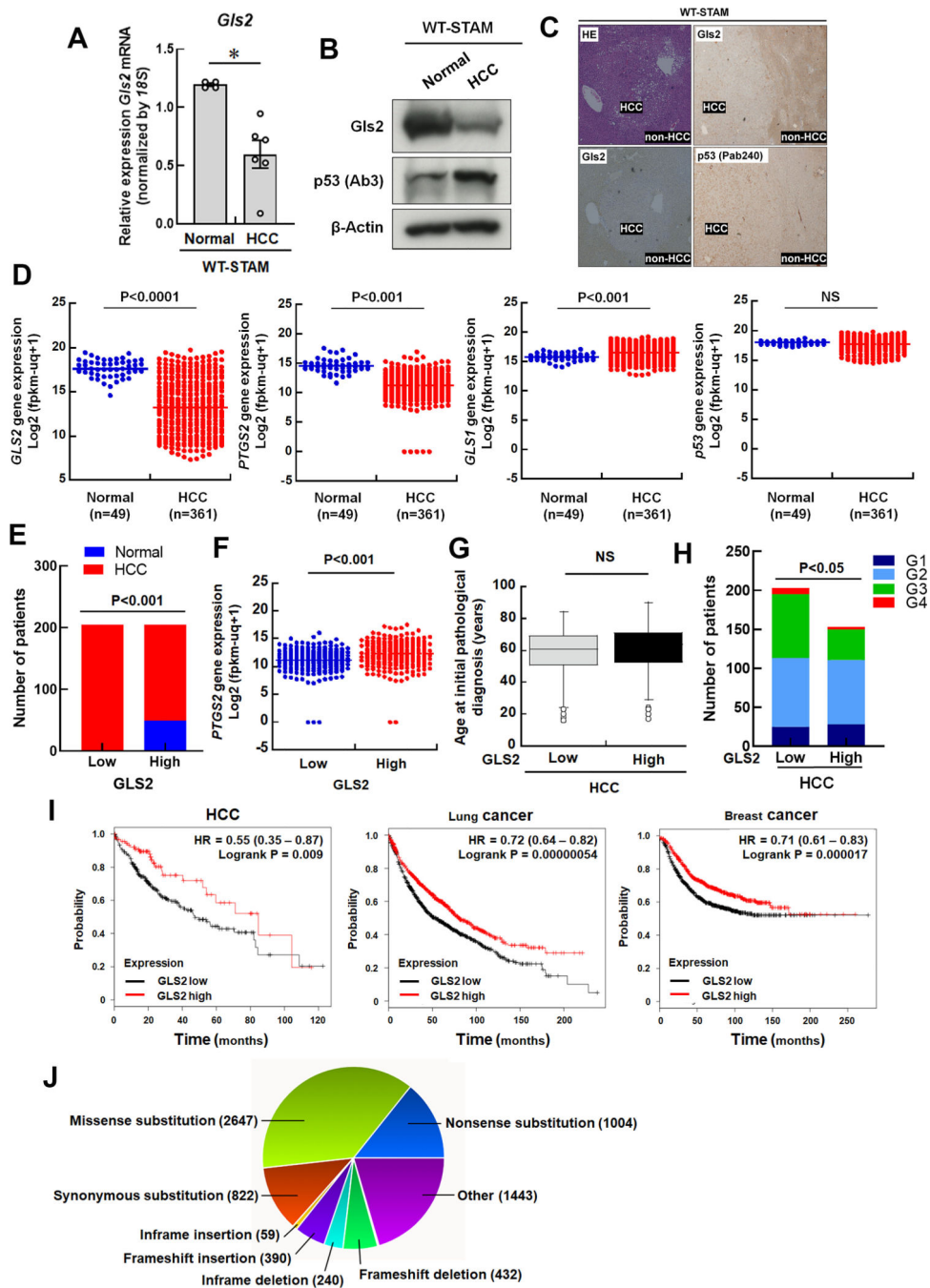


**Figure 6. GLS2 expression levels are decreased in both mice and human HCC and these levels are correlated with malignancy and poor prognosis**

**A**, RT-qPCR analysis of *Gls2* expression in liver tissues from HCC stages (22 weeks, n=6) compared to normal stage (6 weeks, n=5) in STAM generated from wild-type mice (WT-STAM). Bar graph depicts means  $\pm$  SEM \*P < 0.05 versus the normal stage. **B**, Western blot analysis of Gls2 or p53 (Ab3) protein expression in the liver from HCC and normal stages in WT-STAM mice. **C**, Immunohisto-chemical analysis of Gls2 and p53 (Pab240) in liver from WT-STAM, mice containing HCC and non-HCC regions. **D**, *GLS2*, *PTGS2*, *GLS1* or *p53*

mRNA expression levels in human HCC samples (HCC) compared to normal liver tissues (Normal) were assessed using the Cancer Genome Atlas (TCGA) database and the GDC portal (<https://portal.gdc.cancer.gov/>). **E**, The numbers of HCC or normal samples from patients in TCGA database were categorized based on *GLS2* expression levels as *GLS2* low (below the median) or *GLS2* high (over the median). **F**, *PTGS2* mRNA expression level was assessed in *GLS2* low or *GLS2* patients. **G-H**, Clinical (age at initial pathological diagnosis in G) and pathological data (histological grades; G1, G2, G3 or G4 in H) in human HCC according to *GLS2* low (n=205) and *GLS2* high (n=205) were extracted from TCGA. **I**, Kaplan-Meier analyses were performed using KM-plotter database ([kmplot.com/analysis/](http://kmplot.com/analysis/)). The graph represents survival curves of patients stratified according to *GLS2* low (black) and *GLS2* high (red) in human HCC, lung cancer and breast cancer samples. **J**, Catalogue of Somatic Mutations in Cancer (COSMIC) analysis in 3256 samples of human hepatocellular carcinoma. The mutation subtypes of *GLS2* from the COSMIC database are shown. Number of mutations for each subtype is shown in parentheses.